Development of Aerodynamic Design Strategies for Human-Powered Vehicles and Streamlined Land Vehicles

by

Trefor Evans

Supervisor: David W. Zingg

University of Toronto
Faculty of Applied Science and Engineering
Division of Engineering Science

April 10, 2014

Abstract

Development of Aerodynamic Design Strategies for Human-Powered Vehicles and Streamlined Land Vehicles

Trefor Evans
University of Toronto
Faculty of Applied Science and Engineering
Division of Engineering Science
2014

In this report, an new method for the practical aerodynamic development of streamlined land vehicles is presented. Using inverse aerodynamic shape optimization, pressure distributions along surface streamlines over a vehicle are designed for extensive runs of natural laminar flow together with an optimal Stratford pressure recovery, then a shape is found to satisfy this pressure distribution. This allows for design of a vehicle with a substantial reduction in drag over vehicles designed by previous methods. The inverse design method also greatly reduces the experience required of the designer, as the distribution is found automatically by adjusting the users initial shape to the closest possible shape which satisfies the extent of laminar flow desired. Additionally, this method will greatly reduce the design lead time of streamlined land vehicle over existing methods which can be very time consuming. An example presented for the design of a new human-powered vehicle demonstrates the effectiveness of the presented method.

Acknowledgments

I would like to thank my supervisor, David W. Zingg, for giving me the opportunity to work under his guidance and for his support of my research topic. His valuable insights formed the starting points of many new ideas.

My sincere thanks to several individuals at the CFD lab who have been helpful throughout this project. I would particularly like to thank Howard Buckley for all his assistance.

I am grateful to the members of University of Toronto Human-Powered Vehicles Design Team for all that our work has done to help me learn and grow over these four years. I would particularly like to thank the team founders; Todd Reichert, Cameron Robertson and Victor Ragusila; not only for the legacy they have begun but for their incredible leadership and all that they have taught me about engineering design. I would also like to thank our team's faculty advisor, Jun Nogami, for all of his support.

Lastly, I would especially like to thank my family for their unwaivering support through all of my wild endeavors.

Trefor Evans
January 20, 2015

Contents

List of Figures

List of Tables

List of Symbols and Abbreviations

Alphanumeric & Calligraphic Symbols

A_{front}	Front view projected area
A_{plan}	Plan view projected area
A_{wet}	Wetted area
AR	Aspect ratio
e	Span efficiency factor
f	Objective function
$C_{d,flat}$	Flat plate drag coefficient
$C_{d,i}$	Induced drag coefficient based on plan view projected area
$C_{d,wet}$	Drag coefficient based on wetted area
C_L	Lift coefficient
C_p	Pressure coefficient
$\bar{C}_p$	Canonical pressure coefficient
$C_{p,min}$	Minimum pressure coefficient
$C_{p,trunc}$	Pressure coefficient value where the pressure recovery is truncated
$C_{p,ideal}$	Ideal pressure coefficient distribution
C_{rr}	Rolling resistance coefficient
C^n	Specification of continuity of a function to its first n derivatives
C_τ	Local shear stress coefficient
C_f	Total skin friction drag
ℓ	Arc length of a streamline
L	Vehicle length
M_∞	Free-stream mach number
q_∞	Free-stream dynamic pressure
r_y	Defined as $\sqrt{x^2 + z^2}$
Re	Reynolds number

S	Stratford-Smith constant
s	Coordinate position along the arc length of a streamline
s_0	Streamwise position of start of pressure recovery
s_t	Streamwise boundary-layer transition location
s_{trunc}	Streamwise location of the pressure recovery truncation
U	Chordwise flow velocity
U_∞	Freestream flow velocity
W	Vehicle weight
χ	Design parameter set
x, y, z	Coordinate axes in the aerodynamic frame (see Figure 4.1)
x_t	x value at the point of transition to a turbulent boundary layer

Greek Symbols

δ	Boundary-layer thickness
δ^*	Boundary-layer displacement thickness
ν	Kinematic viscosity
ϕ	Defined as $\arctan\left(\frac{x}{z}\right)$
ρ_∞	Freestream flow density
θ	Boundary-layer momentum thickness

Abbreviations

CAD	Computer-Aided Design
CFD	Computational Fluid Dynamics
HPV	Human-Powered Vehicle
IHPVA	International Human-Powered Vehicle Association
NLF	Natural laminar Flow

Chapter 1

Introduction

This research project involves the study of methods to reduce the aerodynamic drag on Human-Powered Vehicles (HPVs), many aspects of which apply to streamlined land vehicles in general. The research focuses on development of a more effective design strategy then the current state of the art to minimize the drag over such vehicles, subject to practical design constraints.

Streamlined land vehicles can have an astounding benefit in efficiency over the automobiles on the road today. Previous HPVs have exceeded speeds of $130km/hr$ on a flat road and have traveled over $90km$ in one-hour [12] all with only the $\sim 0.5hp$ which an athletic human being can sustain.

Additionally, it may be noted from [12] that the world one-hour distance records for Human-Powered Vehicles have been continuing to increase at a rapid rate over the past 30 years. As can be seen in Figure 1.1, it is evident that this trend shows no sign of reaching an apex which suggests that the design of these vehicles have not yet converged towards an optimal design configuration. This seems to indicate that current HPVs may still have the potential for great gains in efficiency. It is similarly evident that the considerably less optimized automotive industry stands to gain even more from similar design strategies in order to provide future forms of viable and efficient land transportation.

Current aerodynamic design strategies for HPVs and streamlined land vehicles require months of work and many design iterations. These iterations typically involve menial shape adjustments however they require a technically skilled individual since an experienced understanding of the aerodynamic flows around the vehicle are essential to make appropriate shape adjustments. Additionally, with all this effort, a truly ideal design is still very difficult to achieve since the design freedom must be limited in order for a designer to stay within a realistic design timeline. More about current design strategies will be discussed in §2.2.

Highly automated design strategies have been a major topic of research in the aerospace

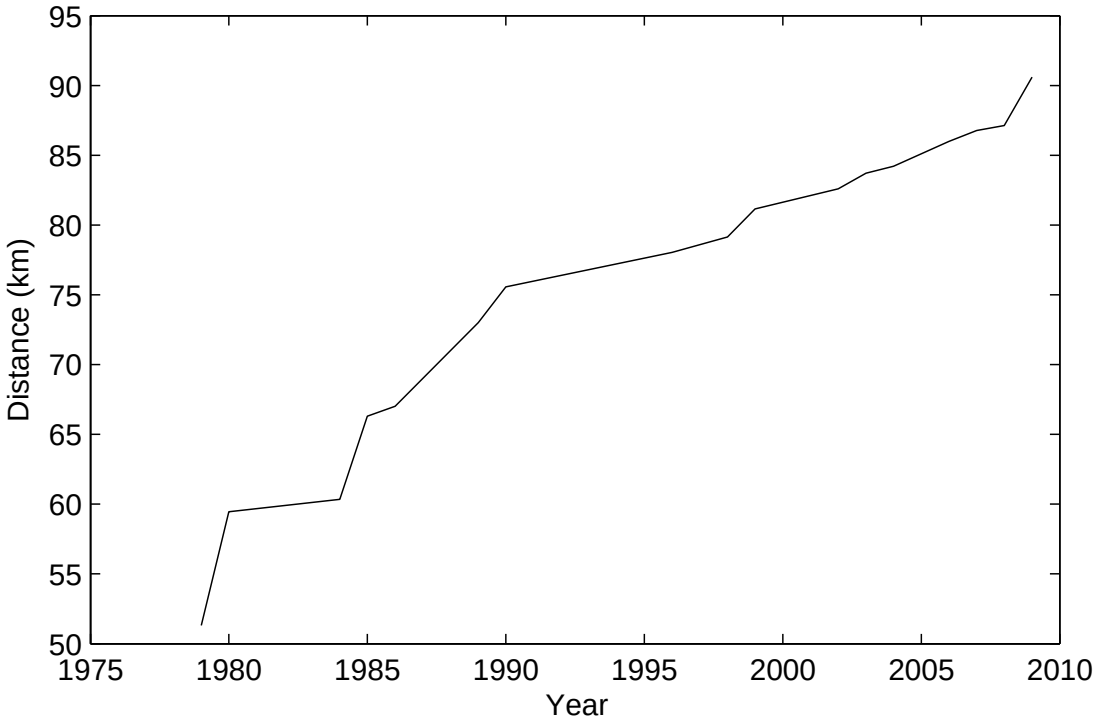

Figure 1.1: IHPVA one-hour endurance record distances [12].

industry for some years. In particular, many of these tools have been developed at the University of Toronto Institute for Aerospace Studies [9, 17], the most relevant development being *Jetstream*, a set of computational tools for the purpose of three-dimensional aerodynamic shape optimization. Unfortunately, *Jetstream* currently has no functionality for three-dimensional aerodynamic shape optimization with laminar-turbulent transition prediction which would be required to minimize a drag objective function for a streamlined land vehicle. Instead, this report will focus on the development of a design scheme utilizing an inverse aerodynamic design approach to determine the shape of a vehicle given a specified surface pressure distribution. This unfortunately requires marginally more experience on the part of the designer, however drag minimization with laminar-turbulent transition is beyond the current-state of the art.

Using the inverse design method proposed allows the designer to shape a vehicle based on the pressure distribution about the body which is directly related to the stability of the laminar boundary layer, the induced drag on the body and the onset of flow separation over the body [13, 22, 24]. This allows the designer to ensure a robust laminar boundary layer over the desired regions of the vehicle and to design an optimal closure for pressure recovery. Useful geometric constraints can also be applied for practical considerations. This will be

discussed further in §4. This method offers substantial benefits in providing great control of many important aerodynamic parameters compared to currently employed design methods. These benefits will be described in §2.2.

1.1 Thesis Objectives

Using the inverse design method described above, a new human-powered vehicle will be developed. This HPV will be a high-performance race vehicle designed to reach the highest possible speed on a closed course with little compromises made for utility. While this will not be designed with utility in mind, the design will feature tight geometric constraints, and extensions to more modular streamlined land vehicles will be made throughout the report. This type of vehicle has been optimized and built by the University of Toronto's HPV Design Team several times in the past. The most successful of these vehicles is *Bluenose* which is currently the 8^{th} fastest vehicle in the world and raced to a top speed of 125.02 km/hr at the World Human-Powered Speed Challenge in 2013 [16]. Extensive design optimization and development went into the design of *Bluenose*, and vehicle testing has demonstrated extensive runs of laminar flow at speed ($\sim 0.6\ x_t/L$). This testing has demonstrated that *Bluenose's* drag values are competitive with the top vehicles in the world. Ultimately, it is expected that *Bluenose* can achieve much higher speeds than those achieved in 2013 as the vehicle crashed at the competition, impairing it for many of its record attempts, and thus maximal speeds were not reached. The goal of this project is to improve upon the design of *Bluenose* by reducing the drag on this reference design. Since *Bluenose* was so optimally designed, such a task would be a great challenge if design was conducted as it had been done in the past. Therefore, this will be a good demonstration of the method's capability.

The designed vehicle will be built by the AeroVelo; however road testing of this design would likely not be complete within the timeline of the project. Instead computational simulation results will be compared between the designed vehicle and *Bluenose*.

Chapter 2

Design of a Streamlined Land Vehicle

2.1 Design Problem Definition

To specify a practical design problem, high level design requirements pertaining to aerodynamics for a general streamlined land vehicle are listed below:

- The vehicle shall have internal flow within the external aerodynamic fairing.
  This could include ventilation to the pilot(s), supply of oxygen for an air breathing engine and for cooling some internal component(s)
- The vehicle shall make mechanical contact with the ground.
  This means the vehicle will likely be in deep ground effect which must be accounted for in the aerodynamic simulation and design.
- Aerodynamic devices and fairings shall not interfere with internal geometric constraints.
  Whether geometric constraints for vehicle structure, mechanical components or pilot ergonomics, these constraints must be adhered to for any practical design.

The goal of this research is to develop a design method to reduce the aerodynamic drag on a vehicle given satisfying the requirements set by a given design problem. The design method will be discussed in §4.

2.2 Historical Design Strategies

Existing methods used to design streamlined land vehicles involve specifying the shape of the vehicle which can then be analyzed aerodynamically and then the process can be reiterated based upon the results. This process will be illustrated in this section and can be considered

the current state of the art as it is used extensively in the design of streamlined land vehicles, particularly in the design of HPV's [3, 19, 27]. The design process is enumerated as follows:

1. Determine geometric constraints of all internal objects which must be placed within the vehicle with CAD software.
2. Determine a preliminary aerodynamic shape around the body using CAD software.
3. Run CFD analysis.
4. Analyze extent of laminar flow, lift and drag (depending on CFD model used).
5. Determine how to improve upon the metrics listed above by adjusting the pressure distribution along streamlines. Adjust the vehicle shape to attempt to facilitate these changes.
6. Return to step 3 and iterate if necessary until the current design point is satisfactory, meeting all constraints and aerodynamic goals.

It is evident that this design process is effectively designing the vehicle in a non-automated inverse aerodynamic approach. Automating the approach could lead to significantly faster turn-around times and a more precisely designed pressure profile. Additionally, adjusting the shape of a three-dimensional surface based on the desired change in a pressure profile often requires great experience on the part of the user to make the connection of how a pressure distribution is altered with a change in shape, whereas the automated design scheme presented in this report would not require this level of experience from the user. Ultimately it would be a substantial improvement over the current state of the art.

Chapter 3

Design Method Scope

This chapter will decompose the components of drag, briefly outline them and mention how they will be taken into account in the design scheme.

3.1 Separation Pressure Drag

This drag component is a result of pressure drag caused by boundary-layer separation from an aerodynamic surface. This component should ideally be zero in the design of a streamlined land vehicle and will be accounted for in the design method by analyzing the pressure gradient along streamlines and ensuring separation does not occur by the Stratford separation criterion extended by Smith for axisymmetric bodies [22]. Stratford and Smith present an analytic formulation which indicates when the boundary layer is on the verge of separation, at which point the wall shear will approach zero. This scheme can be used for an optimal pressure recovery curve at the rear of the vehicle while preventing boundary-layer separation. This scheme will be described in greater detail in §4.3.2.

3.2 Viscous Shear Drag

The viscous shear drag is the most substantial component of drag which acts upon a streamlined land vehicle [24] and is caused by viscous shear forces acting tangentially on the surface of the vehicle within the boundary layer. At the Reynolds numbers that most streamlined land vehicles operate at, x_t/L can be quite large, and extensive runs of natural laminar flow are possible which have significantly less drag than a turbulent boundary-layer.

In order to design for extensive runs of natural laminar flow, a decreasing pressure gradient will have the favorable effect of damping-out disturbances in the laminar boundary layer

that would otherwise amplify and destabilize the flow, leading to transition to a turbulent boundary layer [26, 15, 24]. The inverse design method presented in this report allows the user to directly vary the target pressure distribution across the vehicle where natural laminar flow is desired.

Depending on the shape of the body, the laminar boundary layer can be forced into transition by other means that are not determined by the pressure profile along the streamlines on the body. Such instability methods include attachment line, cross flow and acoustic instabilities [21]. These instabilities will not be accounted for in the design scheme however their effect can be reduced by ensuring the vehicle does not have a highly swept or sharp nose and by acoustically damping the aerodynamic fairing from road or engine vibrations [24, 27].

Additionally, it may be noted that accelerating the flow across a body leads to a higher skin friction drag, C_τ. The reason for this is two-fold: accelerating flow on the surface leads to a decrease in boundary-layer thickness, δ, and results in higher flow velocities throughout the boundary layer [2, 24]. Both of these contribute to increasing the velocity gradient off of the aerodynamic surface, thus increasing C_τ. While it is necessary to accelerate a laminar boundary layer (as was mentioned above), accelerating a turbulent boundary layer should be avoided. What this means for design is that the boundary layer should transition at the point of minimum pressure on the body. The formulation of the ideal pressure distributions which will be used in the inverse design process will allow this concept to be incorporated. Further discussion on the development of a pressure distribution will proceed in §4.3.1.

One further point which should be made about the importance of maintaining laminar flow across the body is the effect it has on the rate of pressure recovery. According to Stratford [23] the closeness to separation on the body is related to the momentum thickness of the boundary layer (θ) at the point of the start of pressure recovery. Anderson [2] presents a relation to calculate the momentum thickness at the trailing edge of a flat plate:

$$\theta_{x=L} = \frac{LC_f}{2} \tag{3.1}$$

Therefore at a point on the body, the momentum thickness of a laminar boundary layer will be $\frac{C_{f,lam\ flatplate}}{C_{f,turb\ flatplate}}$ times thinner than a turbulent one. According to Stratford, this means that the boundary layer will be $\sqrt{\frac{C_{f,turb\ flatplate}}{C_{f,lam\ flatplate}}}$ times closer to separation for a boundary layer which was turbulent verses one which was laminar up to the point of pressure recovery. This value is often much greater than 1. While the pressure gradient does play a role in the development of θ over the three-dimensional body compared to a flat plate, the effect appears to not be great since the super velocity over a three-dimensional body is slightly canceled by its nose stagnation point (based upon analysis of Equation 4.3 which takes this

into account). Ultimately, it is evident that a greater extent of natural laminar flow leads to a thinner momentum boundary layer thickness and thus allows a steeper pressure recovery curve and therefore a shorter tail which makes for a more efficient closure at the rear of the vehicle.

3.3 Boundary-Layer Pressure Drag

The boundary layer creates some pressure drag which acts upon a body caused by the the boundary-layer thickness. The contribution of this drag effect is often small and cannot be modelled without a viscous flow solution and greater computational expense then solving the inviscid Euler equations. This effect will be evident in any design and is rarely addressed using other design methods. It will not be directly considered here however the goal mentioned in the viscous shear drag section (§3.2) is to maximize the extent of the laminar boundary layer which not only reduces the viscous shear drag but also reduces the boundary-layer thickness at the trailing edge and subsequently reduces the boundary-layer pressure drag as well. Additionally, experimental data of the boundary-layer thickness (δ) at the trailing edge of an airfoil by Steuper is presented by Schlichting [21] and the deviance in Steuper's data relative to δ predicted by a flat plate approximation deviate by only $\pm 10\%$ which suggests that the effect of the pressure gradient over the vehicle on δ is not great (assuming the flow remains attached). This suggests that little can be done to design for this component of drag with a change in shape even if other means were employed.

3.4 Induced Drag

Induced drag is commonly associated with the production of lift over three-dimensional body. Assuming the vehicle to be symmetric left to right and that the vehicle will rarely drive in a significant crosswind, only vertical aerodynamic forces upwards and downwards will be considered. A vehicle intended for travel on land can rarely be designed to generate vertical lift efficiently because it would be a challenge to navigate any vehicle of appreciable aspect ratio on any open road. Still, in order to account for the full benefit of generating vertical lift, the rolling resistance of the vehicle must be considered. Thus considering only the rolling resistance and induced drag on a vehicle, applying linear aerodynamics and rolling resistance relations from Tamai [24], the drag can be approximated as

$$D = C_{rr}(W - q_\infty A_{plan} C_L) + \frac{q_\infty A_{plan} C_L^2}{\pi e AR} \tag{3.2}$$

The minimum of Equation 3.2 with respect to C_L is

$$C_L = \frac{C_{rr} AR\pi e}{2} \tag{3.3}$$

Given low rolling resistance tires ($\mathcal{O}(C_{rr}) = 10^{-3}$) and a typical aspect ratio of previous HPVs ($\mathcal{O}(AR) = 10^{-1}$) then $\mathcal{O}(C_L)$ should be $\sim 10^{-4}$ and can generally be taken as zero. However, since *Jetstream* accepts C_L equality constraints for aerodynamic shape optimization, this optimal C_L can be accounted for in the design scheme.

3.5 Interference Drag

Interference drag includes aerodynamic drag associated with manufacturing limitations and defects as well as ventilation drag. At the aerodynamic design stage of a streamlined land vehicle, manufacturing concerns cannot reasonably be taken into account. Additionally, it was determined during previous work that it is possible to facilitate sufficient ventilation within an existing streamlined body with negligible effects on drag. This was determined both from road testing conducted by the University of Toronto's HPV Design Team, from CFD simulations conducted by Cervelo Cycles in conjunction with the University of Toronto's HPV Design Team as well as from various other sources [4, 27, 24]. Therefore, modeling the effects of ventilation will be neglected in this study which greatly reduces the computation domain to solely external flows.

Chapter 4

Inverse Aerodynamic Design Method

The inverse shape optimization has been conducted using *Jetstream's* design tools; however additional tools were necessary to both analyze and specify how to improve a vehicle before an inverse optimization is run. An outline of the design process as well as all of the tools developed for the design method are outlined in this chapter. The design of *Eta* will serve as an example for the steps outlined in the following sections.

4.1 Design Method Outline

The design process is enumerated as follows with reference to respective sections where aspects will be discussed in more detail:

1. Determine geometric constraints of all internal objects which must be placed within the vehicle with CAD software.

2. Determine a preliminary aerodynamic shape around the body using CAD software.

3. Solve the Euler equations around the preliminary vehicle shape in *Jetstream*. An overview of *Jetstream*'s flow solver is discussed in §4.4.1.

4. Analyze the pressure distribution over the body along surface streamlines. This is discussed in §4.2.

5. Determine the desired pressure distribution which satisfies the amount of laminar flow required but is similar to the pressure distributions at the previous design point. Output this target pressure distribution for the inverse optimization case. This is discussed in §4.3.

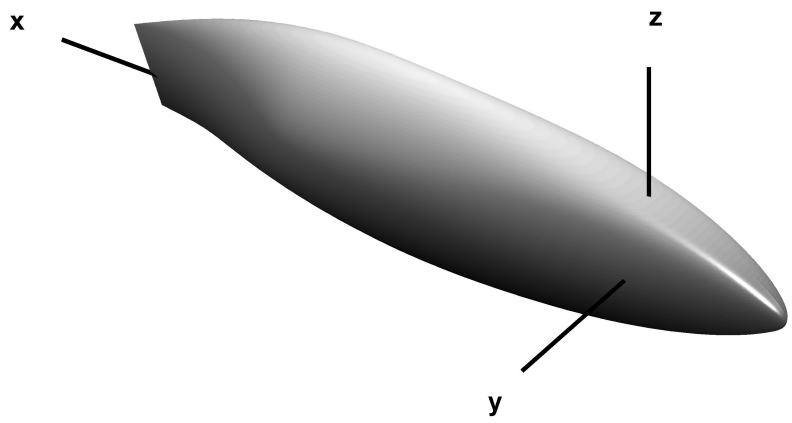

Figure 4.1: The coordinate frame used in this report. The origin is concentric with the bottom bracket of the vehicle on the symmetry plane.

6. Run the inverse optimization case in *Jetstream* until satisfactory convergence. For an overview of *Jetstream*'s inverse optimization see §4.4.

7. Return to step 4. Iterate if necessary until the current design point is satisfactory, meeting all constraints and aerodynamic goals.

Note the similarity to the historical design method described in §2.2. The 2 schemes are very similar, differing mainly by the automation step in evaluating the inverse design.

As the inverse design optimization process is already well established within *Jetstream*, its overview will be very high level and will not go into great detail. This chapter will mostly focus on steps 4 and 5 of the process outlined above, which is a crucial part of the design scheme that involves the user. This step takes the flow solution of the current design as an input and outputs the target pressure distribution to be used to define the objective function for the inverse design optimizations (see §4.4.2).

Lastly, for reference, the coordinate frame used is shown in Figure 4.1.

4.2 Initial Design Point

To begin the design process outlined in §4.1, an initial geometry as well as the flow solution around it must be found. Once the Euler equations have been solved around this original design, the pressure distribution over the body and the streamlines can be analyzed. The streamlines for the initial design point of *Eta* are shown in Figure 4.2. Figure 4.2 also shows the desired boundary-layer transition location and point of pressure recovery for *Eta*. The boundary-layer transition location extends forward across the bottom of *Eta* due to the spreading of boundary-layer transition line caused by an appendage which will be present when *Eta* is constructed. This appendage is not present in the analyzed geometry (for simplicity, since it is will be a thin appendage and will be assumed to not have a great effect on the global flow solution) however it will be a front wheel fairing which can be seen on the University of Toronto's HPV Design Team's vehicle *Vortex* in Figure 4.3. In Figure 4.3, the transition line can be seen spreading across the surface from the front wheel fairing as indicated by shear fluid visualization (using the method discussed in §4.3.1). The transition line is also marked by a black line for clarity. This phenomenon is discussed by Tamai and a spreading angle is typically found to be between $12 - 15^\circ$ across the surface of the vehicle [24].

Additionally, the C_p distribution across the initial geometry can be seen in Figure 4.4 and the pressure distribution along the surface streamlines can be seen in Figure 4.5.

Another useful parameter to plot for analysis is the Stratford value to determine how close the flow is to separation at any point along a streamline (The Stratford criterion is outlined in §4.3.2). The Stratford criterion plotted across the surface streamlines of the initial geometry of *Eta* is shown in Figure 4.6.

This process of displaying this data has been automated in Matlab, so given the files output by *Jetstream*, plots of the pressure distribution and Stratford criterion can be displayed immediately.

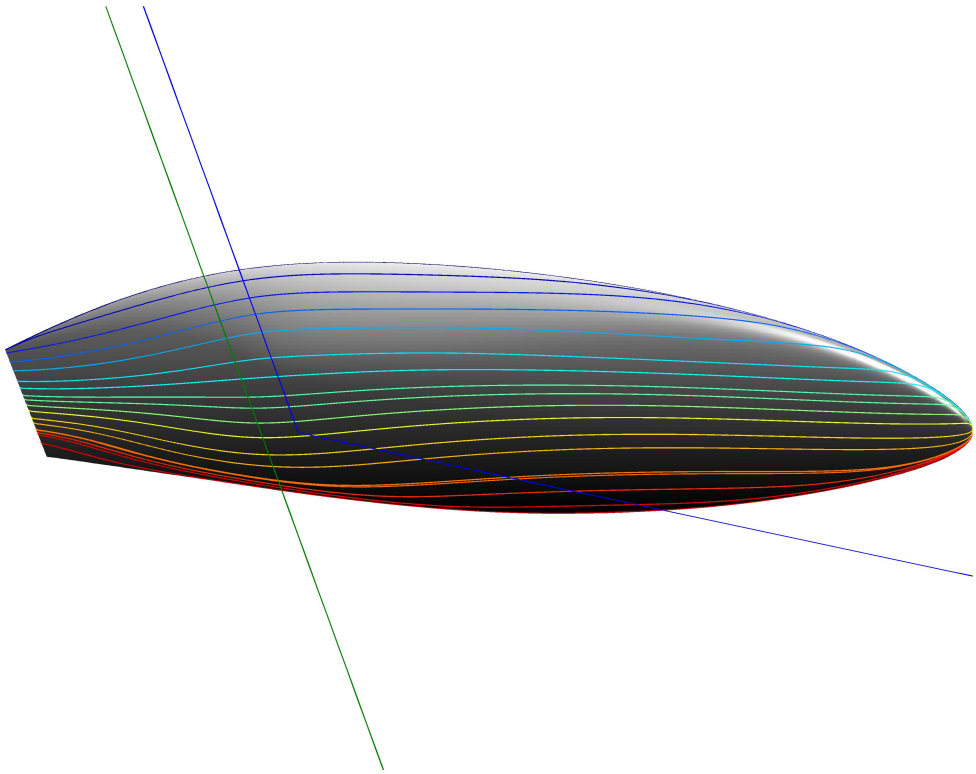

Figure 4.2: Surface streamlines across the initial design point. The colours of the streamlines correspond to the colours in Figures 4.5 and 4.10. Note the lines indicating the desired transition point from a laminar to turbulent boundary layer and the desired point of the start of pressure recovery. For this flow solution, inviscid flow was assumed and $M_\infty = 0.1$.

Figure 4.3: Shear fluid visualization on the University of Toronto's HPV Design Team's *Vortex* at $U_\infty = 80km/hr, \rho = 1.13kg/m^3$ at Ford's Michigan Proving Grounds, Romeo, MI. The shear fluid visualization method is discussed in 4.3.1. The black line indicates the boundary-layer transition line.

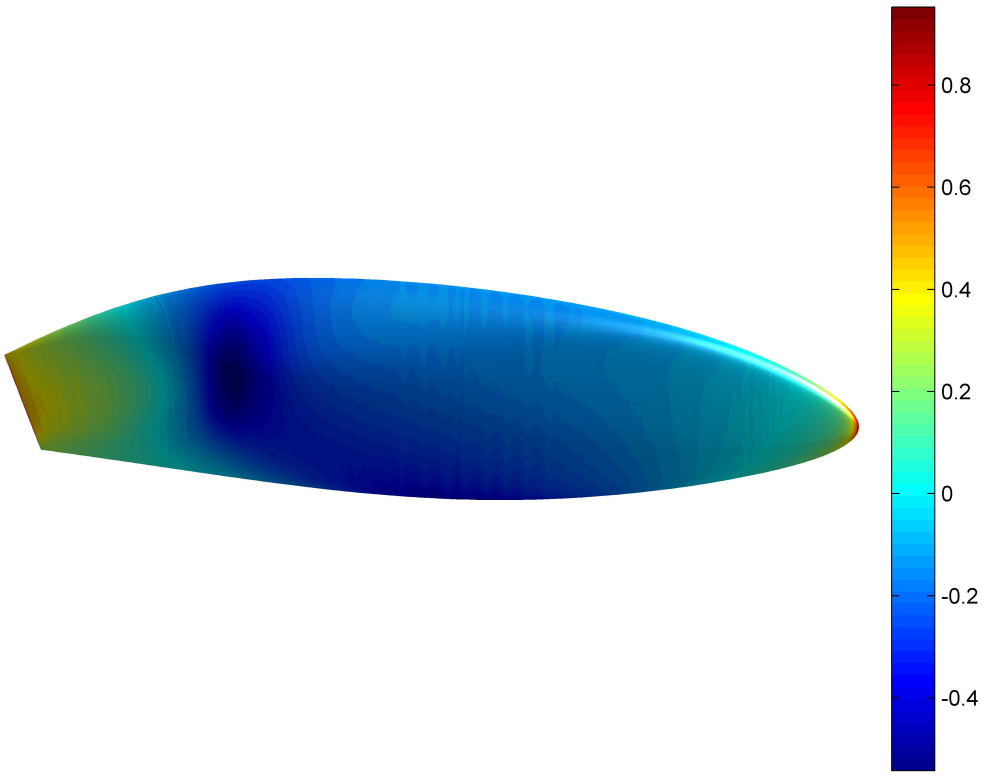

Figure 4.4: C_p distribution plotted on the surface of the initial design point. For this flow solution, inviscid flow was assumed and $M_\infty = 0.1$.

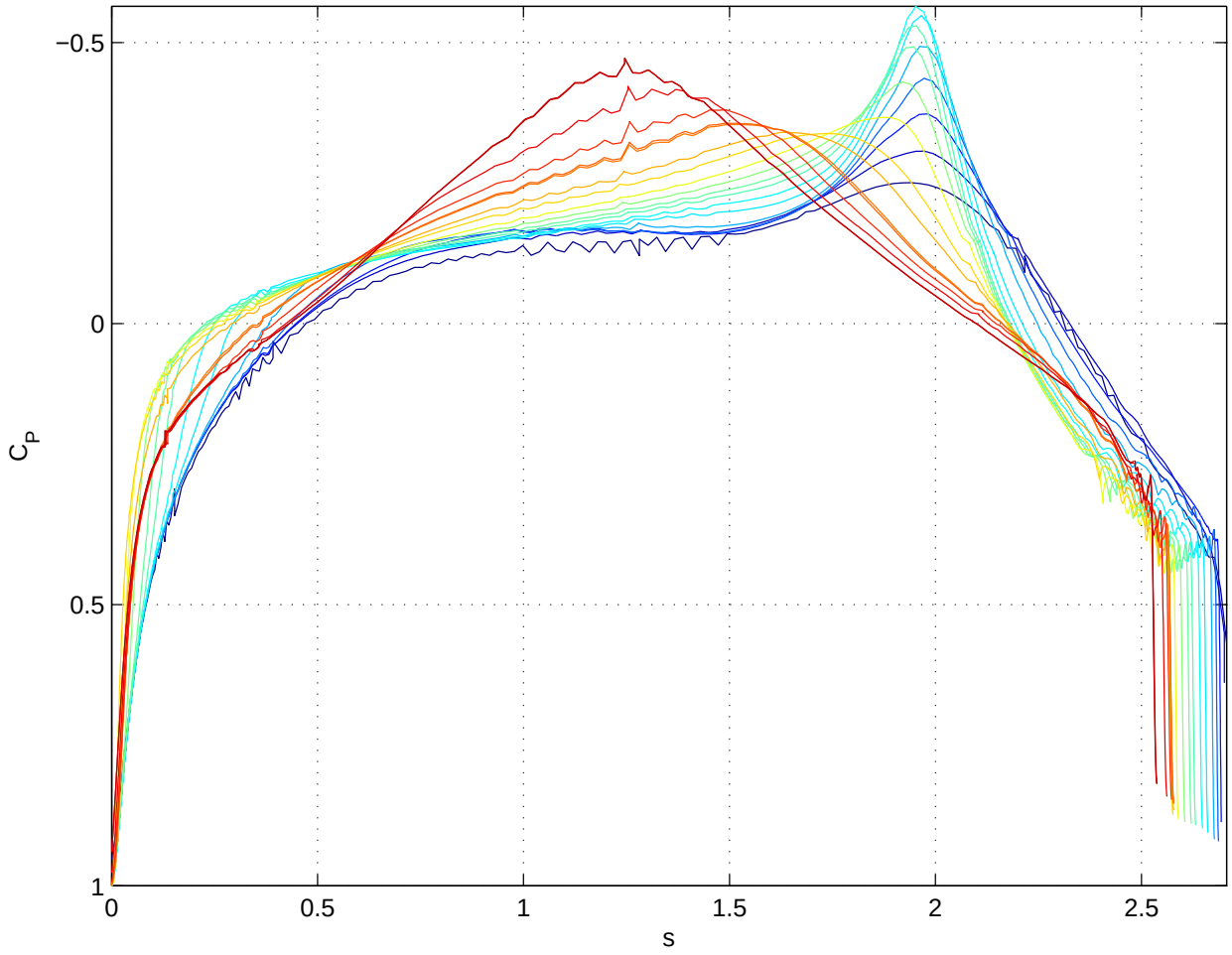

Figure 4.5: Pressure coefficient distribution, C_p verses streamline length, s across the aerodynamic surface of the original geometry. The streamline colours correspond to those shown in Figure 4.2. For this flow solution, inviscid flow was assumed and $M_\infty = 0.1$.

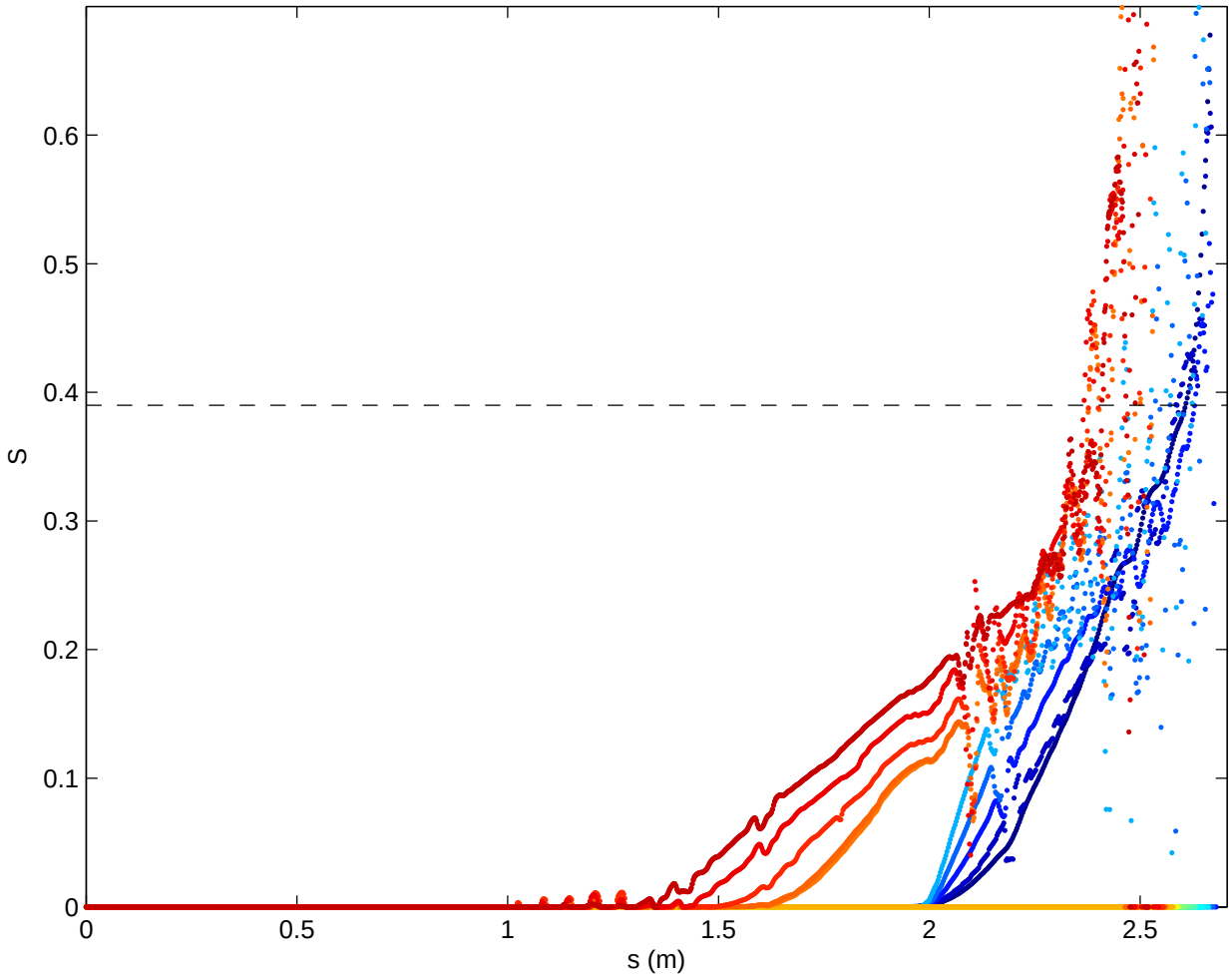

Figure 4.6: Stratford value, S verses streamline length, s across the aerodynamic surface of the initial design point. For this analysis, $U_\infty = 50km/hr, \rho_\infty = 1.21kg/m^3$ and laminar flow is assumed until the transition line shown in Figure 4.2 or the point of $C_{p,min}$, whichever comes first. These conditions relate to the lowest Reynolds number deemed acceptable for flow separation on *Eta*. The streamline colours correspond to those shown in Figure 4.2. For the flow solution, inviscid flow was assumed and $M_\infty = 0.1$.

4.3 Pressure Distribution Design

The pressure distribution design stage involves specifying an improvement to the current pressure distribution (determined from a flow solution of the current shape) and outputting a new target distribution. To design a new target distribution, pressure profiles will be designed along streamlines then interpolated over the entire body. This process is outlined in the following sections.

4.3.1 Streamline Pressure Profiles for NLF

As was mentioned in §3.2, the extent of NLF and thus the amount of viscous shear drag is largely related to the pressure profiles along the streamlines of the vehicle. This section will discuss the formulation of improved target pressure profiles over the portion of the vehicle where laminar flow is desired.

References for target pressure distributions include data from well designed and throughly tested two-dimensional airfoils intended to achieve extensive runs of natural laminar flow. Such airfoils include the NACA 6-Series airfoils [1]. Due to the three-dimensional nature of flow around streamlined land vehicles, the three-dimensional body be much thicker than its two-dimensional counterpart, given a pressure distribution. This is simply caused by three-dimensional pressure relief around the body. This means that a three-dimensional body can typically have a smaller pressure spike over the nose then would be possible on a two-dimensional airfoil due to the undesirable stall characteristics of excessively sharp noses. Therefore, for the design of a three-dimensional pressure profile, a NLF airfoil can be modified to have a smaller leading edge radius and its corresponding pressure profile can be analyzed using airfoil design software such as XFOIL [5]. This adjusted airfoil will typically have a more robust laminar boundary layer than the unmodified airfoil because it allows a steeper favorable (negative) pressure gradient across the main body of the airfoil. The two-dimensional boundary-layer analysis in XFOIL may lead to accurate transition prediction over a three-dimensional body provided the boundary layer transitions naturally. In fact the result will be comparable to many commercial packages such as VSAERO, QUADPAN or CMARC which solve the two-dimensional boundary-layer equations along streamlines in three-dimensional flow [25, 7]. Given a robust pressure profile developed in two-dimensions, the equivalent profile may be used as a target for three-dimensional analysis. The pressure profile parameterization described in §4.3.3 generates profile shapes determined from such an analysis as described here.

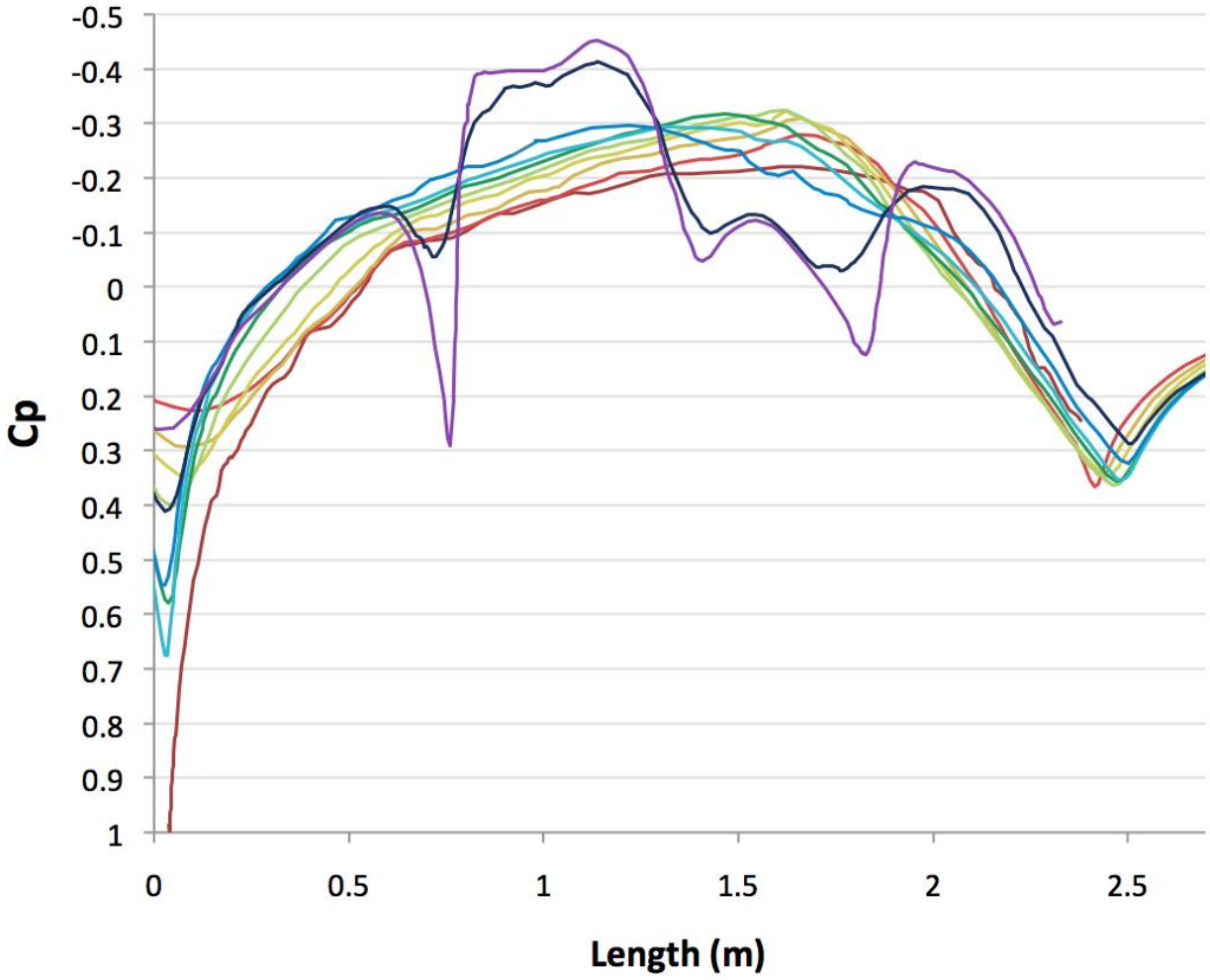

Figure 4.7: C_p verses x along surface streamlines over *Bluenose*.

Validation of Pressure Profile Design for NLF

Bluenose was designed with a similar pressure profiles in its laminar flow region as described above. These profiles can be seen in Figure 4.7.

On road experimental testing was conducted on *Bluenose* by the University of Toronto's HPV Design Team during the summer of 2013 to determine the extent of laminar flow. Shear fluid visualization was used for this analysis which was conducted by spraying automatic transmission fluid onto the surface of the vehicle such that distinct "splotches" could be seen on the white vehicle. These "splotches" create streaks as they are transported by the surface shear. Results of the test at $100km/hr$ is shown in Figure 4.8. The extent of laminar flow can be determined by observing the angle of the fluid's streaks across the surface of the vehicle since in the absence of surface shear, the streaks would move straight downwards due to gravity. As the boundary layer grows and thickens across the body, the surface shear

Figure 4.8: Shear fluid testing over *Bluenose* at $U_\infty = 100km/hr$, $\rho_\infty = 1.13kg/m^3$.

decreases however it is evident near the line traced on the figure that there is a sudden increase in surface shear indicating transition to turbulence. It is evident that $x_t/L \approx 0.6$ on the side of the vehicle which corresponds to the position of minimum pressure in Figure 4.7. It is also evident from the figure that transition is seen spreading from the interface of the windscreen which was likely due to surface imperfections at this point which caused the laminar boundary layer to destabilize. Such a feature will not be present in *Eta* since the vehicle will use a camera system for pilot vision as opposed to a windscreen.

Figure 4.8 fairly effectively demonstrates the robustness of the laminar boundary layer on *Bluenose* in a real world scenario with road vibrations, representative free-stream turbulence and, of course, full three-dimensional effects. Additionally, the test shown in Figure 4.8 was ran an equivalent Reynolds number to what the vehicle would experience at maximum speed at the World Human Power Speed Challenge in Battle Mountain, Nevada due to corrections for altitude density.

Lastly, it is worth mentioning that although the pressure profiles across *Bluenose* were val-

idated from this study, the C_p distribution across *Eta* were designed even more conservatively. For *Bluenose*, all surface streamlines have $\frac{dC_p}{ds} \approx -0.2299m^{-1}$ in the laminar region while *Eta* has a much steeper favorable pressure gradient magnitude across its body even though the extent of laminar flow is greater. For the final design of *Eta*, (described in §5) the surface streamline with the minimum favorable pressure gradient magnitude gives $\frac{dC_p}{ds} = -0.2378m^{-1}$ in the laminar region with most of the streamlines having an even greater gradient magnitude than this. This greater favorable pressure gradient magnitude will help to ensure the damping of instabilities in the laminar boundary layer within *Eta* even more so than in *Bluenose*.

4.3.2 Streamline Pressure Recovery

As mentioned in §3.1, the Stratford separation criterion extended for axisymmetric bodies will be used to design an optimal pressure recovery closure while avoiding boundary-layer separation [22]. This criterion states that separation will occur when

$$\bar{C}_p \frac{\sqrt{s' \frac{d\bar{C}_p}{ds'}}}{(10^{-6}Re)^{\frac{1}{10}}} > S = \text{const.} \tag{4.1}$$

in the pressure recovery region. The prime $(\cdot)'$ denotes the position of equivalent momentum thickness on a body with partly laminar, partly turbulent boundary layers and a variable pressure distribution to that of a turbulent flat plate. A primed value can be determined by the following relation:

$$(\cdot)' = (s_0^* - s_0) + (\cdot) \tag{4.2}$$

where s_0^* is the position on a turbulent flat plate with equivalent momentum thickness to the position of the start of pressure recovery on a streamline with partly laminar, partly turbulent boundary layers and a variable pressure distribution. It can be calculated as follows for a given streamline [23]:

$$\frac{s_0^*}{\ell} = \frac{\dfrac{81.60}{\left(\frac{U_\infty \ell}{\nu}\right)^{5/12}} \left[\displaystyle\int_0^{s_t/\ell} \left(\frac{U}{U_\infty}\right)^5 \left(\frac{\sqrt{y^2+z^2}}{\ell}\right)^2 d\left(\frac{s}{\ell}\right) \right]^{7/12} + \displaystyle\int_{s_t/\ell}^{s_0/\ell} \left(\frac{U}{U_\infty}\right)^{3.33} \left(\frac{\sqrt{y^2+z^2}}{\ell}\right)^{7/6} d\left(\frac{s}{\ell}\right)}{\left[\left(\frac{U}{U_\infty}\right)^3 \left(\frac{\sqrt{y^2+z^2}}{\ell}\right)\right]_{s=s_t}^{7/6}} \tag{4.3}$$

Note however that this assumes the turbulent flat plate flow is fully developed at s_0. Therefore if transition is followed immediately by a steep pressure rise then this relation would only be partially correct. As a result, the pressure profile should be designed with this in mind however if extensive laminar separation is seen on the final vehicle, transition can be forced by surface roughness or a small surface step just before transition with a negligible drag penalty.

Lastly, $\bar{C}_p$ is the canonical pressure coefficient and is defined as

$$\bar{C}_p = \frac{C_p - C_{p,min}}{1 - C_{p,min}} \tag{4.4}$$

Since the boundary layer is typically quite thin at the Reynolds numbers that streamlined land vehicles operated at, the pressure at the edge of the boundary layer for real attached flow should be very similar to that predicted by the Euler equations. Therefore, using the associated pressure profiles will be valid for the pressure recovery analysis mentioned.

Smith's validation studies of Stratford's criterion for axisymmetric bodies suggest that $S = 0.39$ suggested by Stratford is quite conservative and a value of $S = 0.50$ is likely a better estimate for separation. However, in order to remain conservative in this research, Stratford's value of $S = 0.39$ will be used.

Note, however that this analysis is only valid where the boundary-layer thickness is very small relative to the thickness of the body; therefore the analysis cannot be used near $x/L \approx 1$. Instead, the Stratford pressure recovery curve will be said to be "truncated" at this point and its analysis can be neglected. Note that this doesn't correspond to truncating a trailing edge in a geometrical sense but rather allowing the pressure to rise faster than is done within the Stratford pressure recovery. This steep pressure rise at the trailing edge is commonly seen near the rear stagnation point of streamlined bodies.

From the differential Equation 4.1, the optimal pressure recovery distribution has been derived given $C_{p,min}$, $C_{p,trunc}$ and s_{trunc} for a given value of S:

$$\begin{aligned} C_p(s') = \Big[&(C_{p,trunc} - C_{p,min})^3 + 3\left\{S(10^{-6}Re)^{1/10}(1 - C_{p,min})^{3/2}\right\}^2 \dots \\ &\dots \{\log(s') - \log(s'_{trunc})\}\Big]^{1/3} + C_{p,min} \end{aligned} \tag{4.5}$$

4.3.3 Streamline Pressure Profile Parameterization and Optimization

Based upon the desired scope of the design method discussed in §3.2 and the pressure profile shapes discussed in §4.3.1 and §4.3.2, a parameterization has been implemented to design a

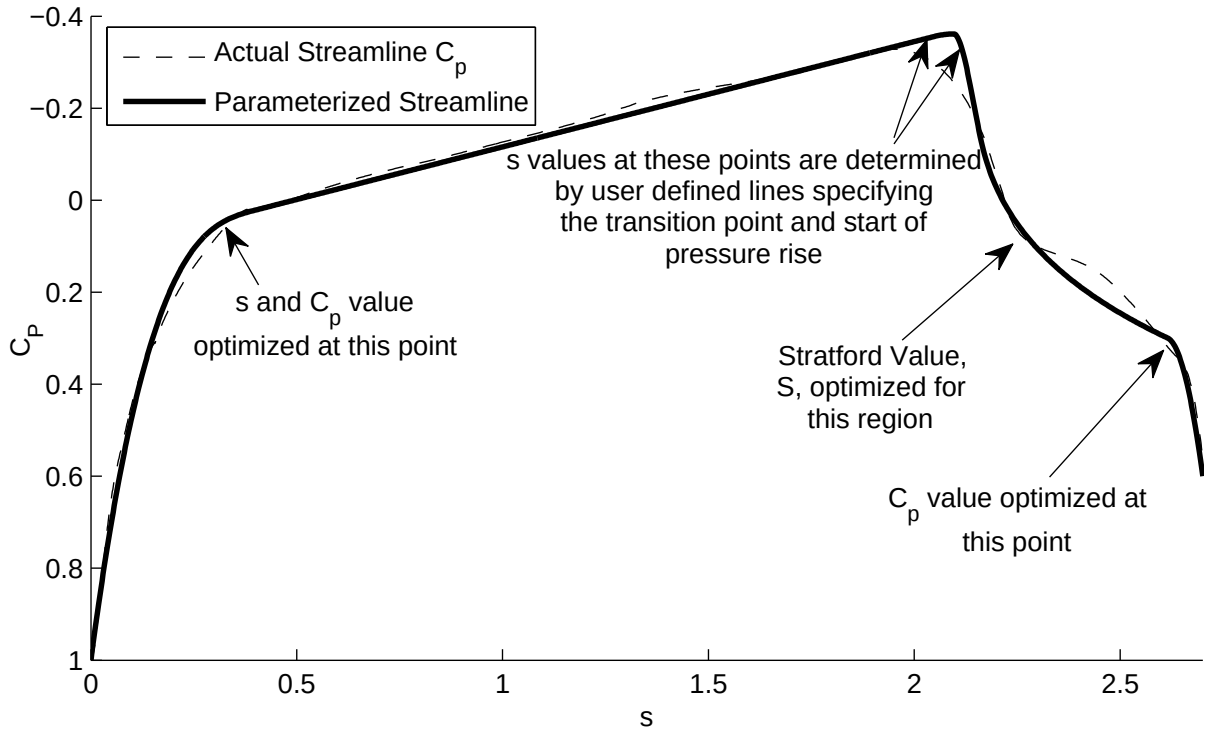

Figure 4.9: Plot of an actual C_p vs s distribution for a vehicle surface streamline with a parameterized NLF streamline fit in a least squares sense.

pressure profile based on four parameters for each streamline. These parameters are optimized using a finite-difference gradient based optimization scheme in order to fit the parameterized streamline to the existing streamline in a least squares sense. An example streamline devised with this parameterization can be seen in Figure 4.9 with the optimization design variables described. The figure specifies the four parameters that are varied in an optimization process in order to fit the parameterized streamline. Note that all other parameters including the s location of the points indicated at the end of the linear region (s_t) and at the start of pressure rise (s_0) are determined by the user before optimization begins. These points are determined by having the user specify lines indicating the extent of laminar flow over the body and the desired point of pressure rise as shown in Figure 4.2. Lastly, the minimum C_p value at the start of pressure rise is determined using the Stratford value given for the pressure recovery region and the C_p value at the start of the pressure recovery truncation.

The purpose of fitting a NLF pressure profile to the existing streamline in a least squares sense is to get the inverse optimization to adjust the original geometry to a laminar flow body with an optimal pressure recovery with as little shape change as possible. This is advantageous because it ensures the highest probability of designing the vehicle to satisfy the

internal geometric constraints (which were of course satisfied by the original geometry) but also to reduce the amount of time the inverse optimization will take to converge (since the optimum would be close to the original design point). Additionally, this scheme allows the design process to be almost entirely automated; minimizing the expertise required of the user as well as the user interface time.

All the regions of the parameterized pressure profile are defined by piecewise cubic polynomials except for the Stratford pressure recovery region which is defined by the relation given in Equation 4.5. C^1 continuity is maintained for the parameterized pressure profile.

The ideal streamwise pressure distributions for the initial design point of *Eta* can be seen in Figure 4.10. The corresponding Stratford values for the ideal streamline C_p distributions are shown in Figure 4.11 at the lowest Reynolds number deemed acceptable for flow separation over *Eta* (where $U_\infty = 50km/hr$ and $\rho_\infty = 1.21kg/m^3$). Additionally, the analysis done of the Stratford values plotted in Figure 4.11 assume that the boundary layer will remain laminar until the transition line shown in Figure 4.2 which is a good assumption at this Reynolds number based on testing of previous HPV's done by the University of Toronto's HPV Design Team. Note, however, that S in the pressure recovery section shown in Figure 4.11 is not exactly at the Stratford specified value of 0.39 for these flow conditions. This was to be conservative in case the inverse optimization does not exactly converge to the target pressure distribution (indeed this was the case as seen in §5). Additionally, it can be seen that the Stratford value is not exactly constant throughout the pressure recovery section as would be optimal. This is due to the fact that a perfect Stratford recovery curve (Equation 4.5) contains an infinite adverse pressure gradient at the start of pressure rise and such a feature is not physically possible. Therefore, for the parameterization, $C_{p,min}$ is brought a distance δ upstream from s_0 (such that the Stratford value ends up below what was desired, not above) and a cubic polynomial is fit from $s_0 - \delta$ to $s_0 + \delta$ where $C_p = C_{p,min}$ and $\frac{dC_p}{ds} = 0$ at $s_0 - \delta$ and C_p and $\frac{dC_p}{ds}$ are found from Equation 4.5 at $s_0 + \delta$. This means that Equation 4.5 is no longer exactly correct, however it still remains close to a perfect Stratford recovery curve and thus will be used due to the elegance of its closed form solution.

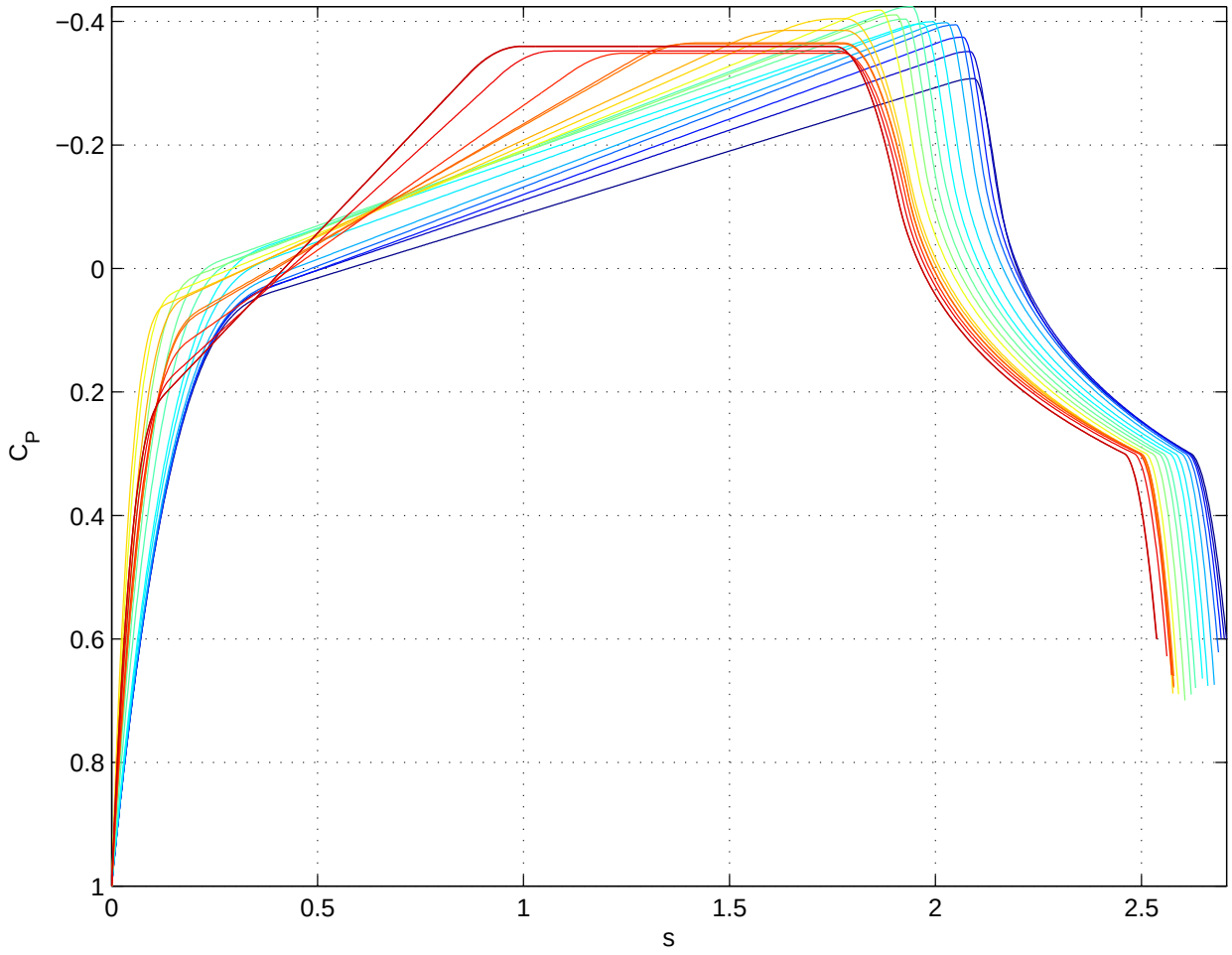

Figure 4.10: Ideal pressure coefficient distribution, $C_{p,ideal}$, verses streamline length, s found for the original design point of *Eta*.

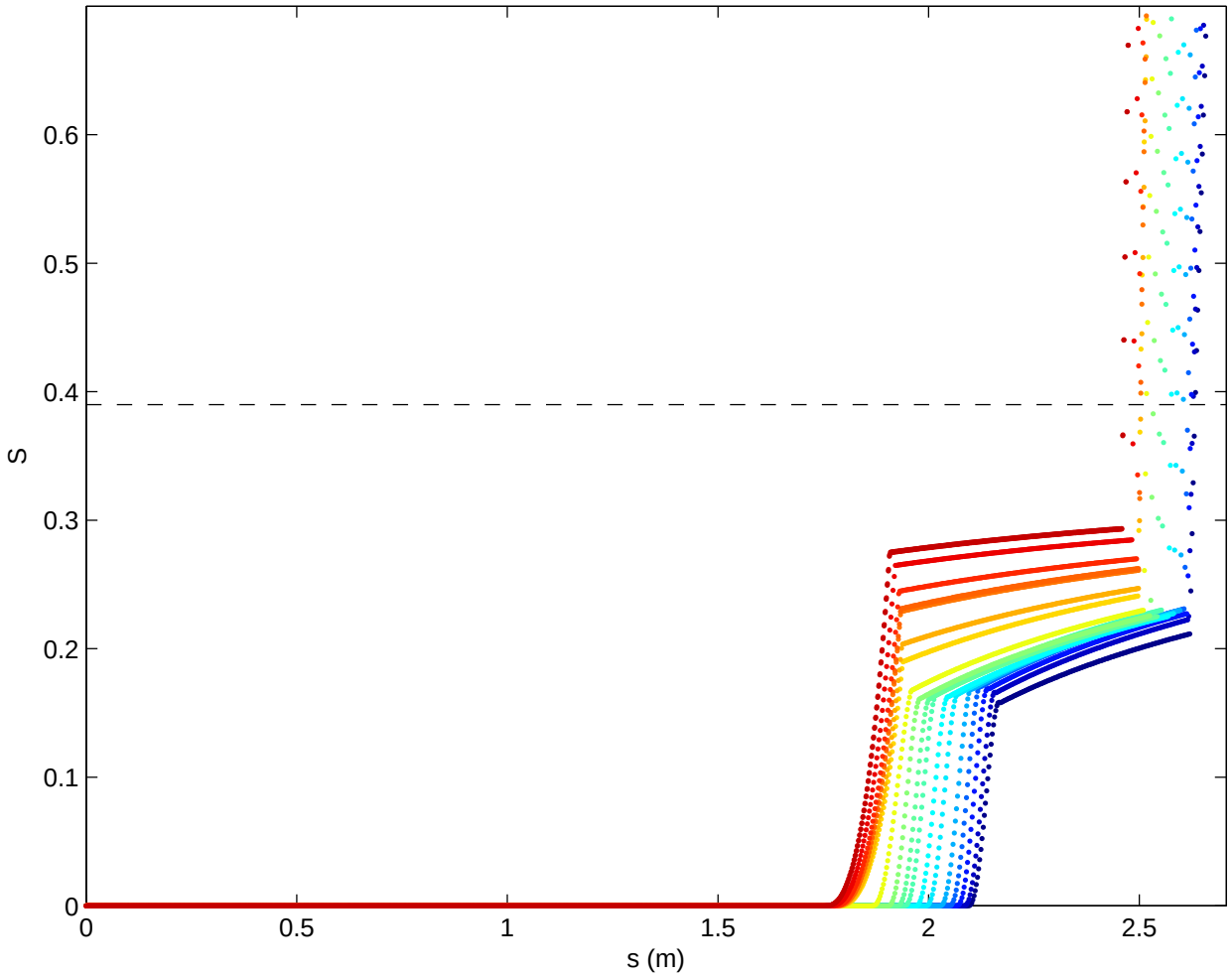

Figure 4.11: Stratford value, S verses streamline length, s across the aerodynamic surface for the ideal streamline C_p distributions shown in Figure 4.10. For this analysis, $U_\infty = 50km/hr, \rho_\infty = 1.21kg/m^3$ and laminar flow is assumed until the transition line shown in Figure 4.2. These conditions relate to the lowest Reynolds number deemed acceptable for flow separation on *Eta*. The streamline colours correspond to those shown in Figure 4.2. Note the only region where the Stratford value exceeds 0.39 is near $s/\ell \approx 1$ where the analysis is not valid. For the flow solution, inviscid flow was assumed and $M_\infty = 0.1$.

4.3.4 Surface Interpolation

Now that the pressure profiles along all streamlines has been determined as described in §4.3.3, the pressure distribution over the entire vehicle surface can be interpolated from the streamline's C_p values across the surface. This was done by fitting a piecewise planar four-dimensional hyper-surface to a finite number of points along the streamlines. This hyper-surface was defined as $C_p = f(y, r_y, \phi)$ where

$$r_y = \sqrt{x^2 + z^2} \tag{4.6}$$

$$\phi = \arctan\left(\frac{x}{z}\right) \tag{4.7}$$

and x, y, z correspond to the coordinates of points on the surface of the vehicle. This hyper-surface was then used to interpolate the C_p value at all of the mesh surface nodes. This will be called $C_{p,ideal}$.

There was many ways the hyper-surface could have been defined however the interpolation method presented here was found to give the best results. $C_{p,ideal}$ found for the initial design point of *Eta* can be seen projected on the original geometry in Figure 4.12.

Now that the ideal pressure distribution is found, the inverse optimization can be run in *Jetstream* which will be discussed in the following section.

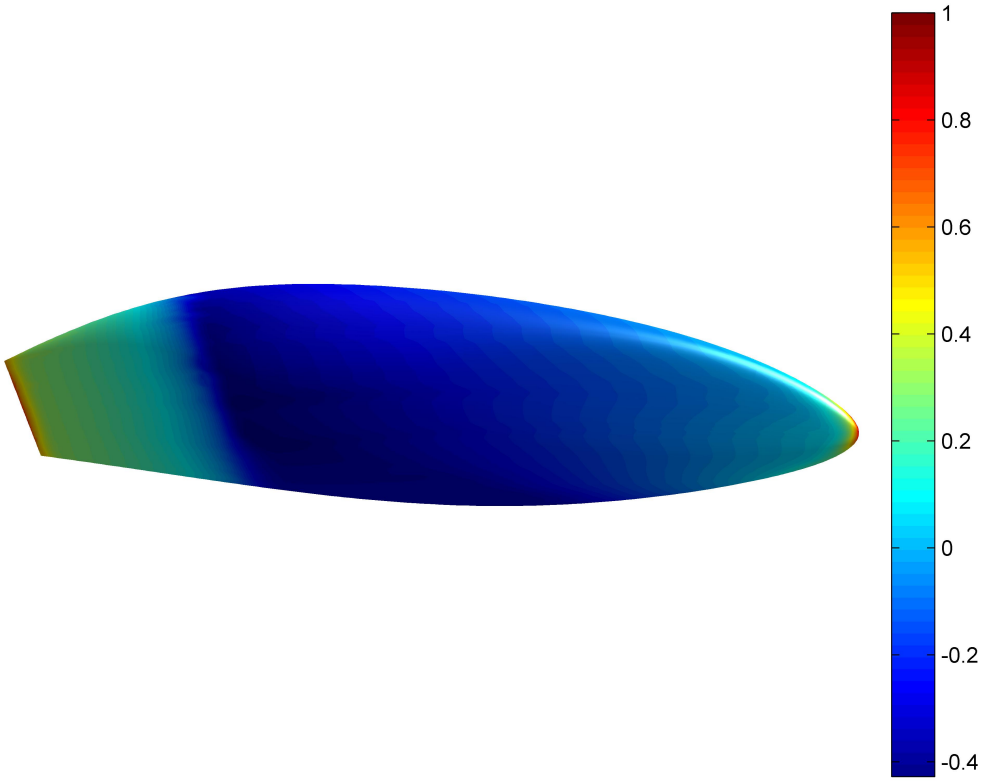

Figure 4.12: Ideal pressure coefficient distribution, $C_{p,ideal}$, found for the original design point of *Eta* projected on the original design point geometry.

4.4 Inverse Shape Optimization in *Jetstream*

Jetstream is an integrated set of computational tools for the purpose of three-dimensional aerodynamic shape optimization and will be used in the research conducted in this study. An outline of *Jetstream's* tools are provided below. Additional information can be found in the accompanying references.

4.4.1 Flow Solution

To evaluate the flow solution, *Jetstream* uses the *Diablo* flow solver, which solves the discretized Euler equations using a parallel Newton-Krylov Solver on a multiblock structured mesh [10].

4.4.2 Objective Function

In the inverse optimization formulation, the shape of the body that matches the target pressure distribution in the least squares sense will be found [18]. The objective function to be minimized is defined as follows:

$$f(\chi) = \frac{1}{2} \sum_{i=0}^{N} \left[C_{p,ideal,i} - C_{p,i}(\chi) \right]^2 \tag{4.8}$$

where N is the number of nodes on the aerodynamic surface, and χ is the vector of design variables (see §4.4.5).

4.4.3 Optimizer

For inverse design optimization, *Jetstream* will be using the gradient-based sequential quadratic programming (SQP) algorithm in SNOPT [8].

4.4.4 Gradient Evaluation

Jetstream computes the gradient of the inverse objective function using adjoint sensitivity analysis. The main advantage of the adjoint method is that the computational cost of the gradient calculation at a design point is nearly independent of the number of design variables. For aerodynamic shape optimization where the number of design variables must be large in order to achieve an optimal design, this is a very powerful tool [18].

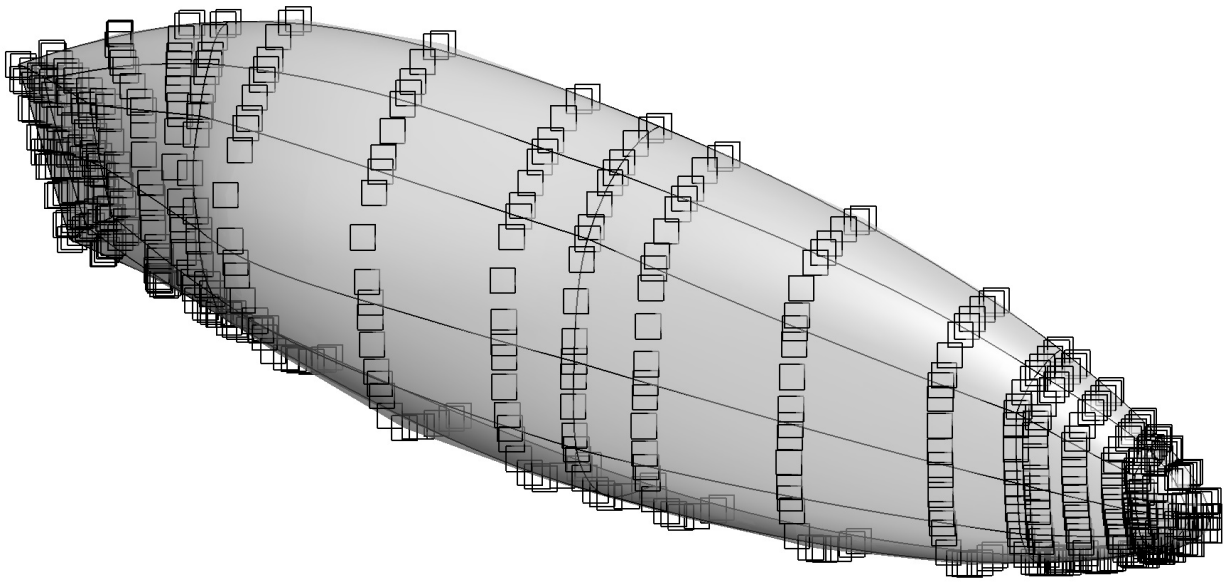

Figure 4.13: Surface control points of used to parameterize the initial geometry of *Eta*

4.4.5 Aerodynamic Surface Parametrization

Basis spline or B-spline volumes are used to parameterize each block of the multiblock grid in the computational domain around the vehicle, and the mesh within the block is then redefined based on the block's parameterization. The translational degrees of freedom of control points within the block which lie on an aerodynamic surface are considered to be design variables [6]. When a surface control point is moved, the block's B-spline volume is adjusted using a grid movement algorithm and thus the mesh can be recomputed based on the new block shape [17].

The surface control points used to parameterize the initial geometry of *Eta* is shown in Figure 4.13. This parameterization has 521 unique control points, many of which have 3 translational degrees of freedom except those on the symmetry plane which are constrained in y. Additionally, one control point is fully constrained. This amounts to a much higher dimensional design space that would be practical to navigate by manually moving control points in the scheme described in §2.2.

4.4.6 Geometric Constraints

Non-linear equality constraints are used to ensure C^1 continuity between face edges on the surface of the vehicle. These constraints impose a collinear constraint between a control point on the edge of a face and the two control points off of the edge on either face.

Additional useful geometric constraints are discussed in §6.2.3.

Chapter 5

Analysis and Results of the Design Method

5.1 Shape Optimization Results

This section will discuss the results of the inverse aerodynamic shape optimization for the design of *Eta*. The objective function value (defined in §4.4.2) decreased to 21.8 % of its initial value throughout the optimization. This reduction can be visualized in Figure 5.1 where the $|C_p - C_{p,ideal}|$ is compared for the final design point to the initial design point.

Figure 5.3 shows the C_p distribution across the surface of the final design. Note its similarity to the $C_{p,ideal}$ distribution shown in Figure 4.12. Similarly, the C_p distribution along the surface streamlines over the final design shown in Figure 5.4 demonstrate great resemblance to the ideal distributions shown in Figure 4.10, particularly in the region where laminar flow is expected.

It can be seen in the bottom image in Figure 5.1 that the largest deviance of the final C_p distribution from $C_{p,ideal}$ is within the pressure recovery region. This is likely due to to the rapid changes in the pressure coefficient gradient in this region (as seen in Figure 4.11). Still, the final design of *Eta* is still seen to satisfy the Stratford-Smith criterion at the minimum acceptable Reynolds number as shown in Figure 5.5.

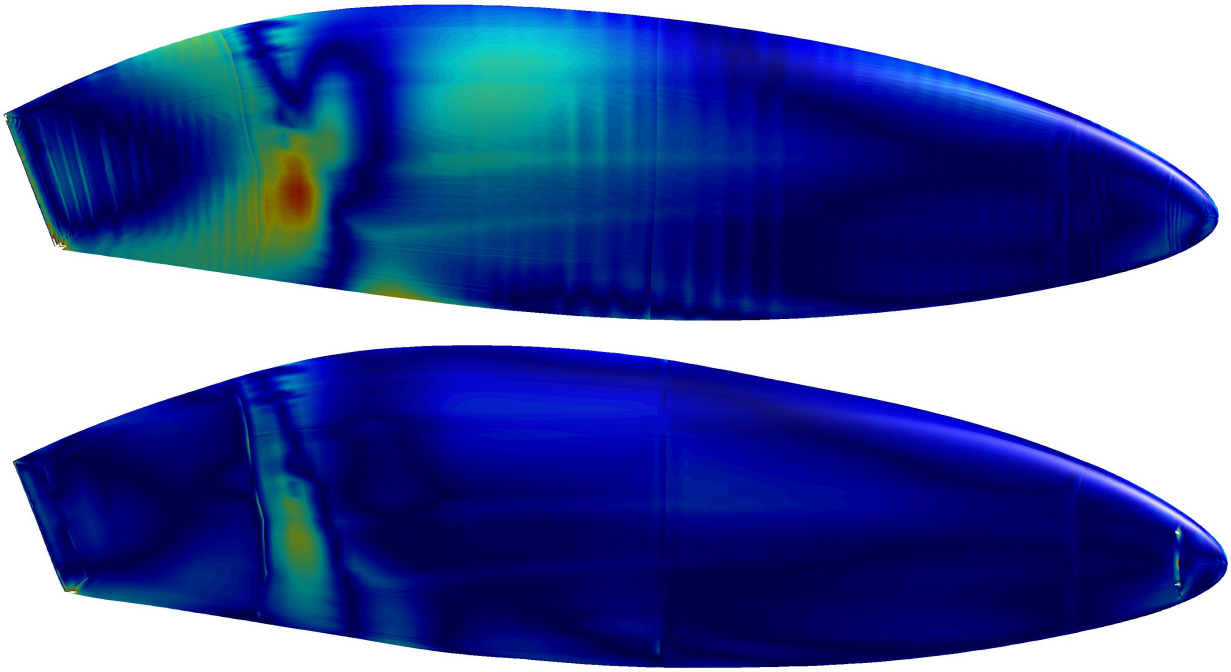

Figure 5.1: $|C_p - C_{p,ideal}|$ at the original design point (top) and final design point (bottom) of *Eta*. Note that the final geometry is much closer to the ideal pressure coefficient distribution. At the block interfaces, discontinuities can be seen in the flow solution. This is due to poor mesh refinement at the block interface however does not affect the quality of the global flow solution.

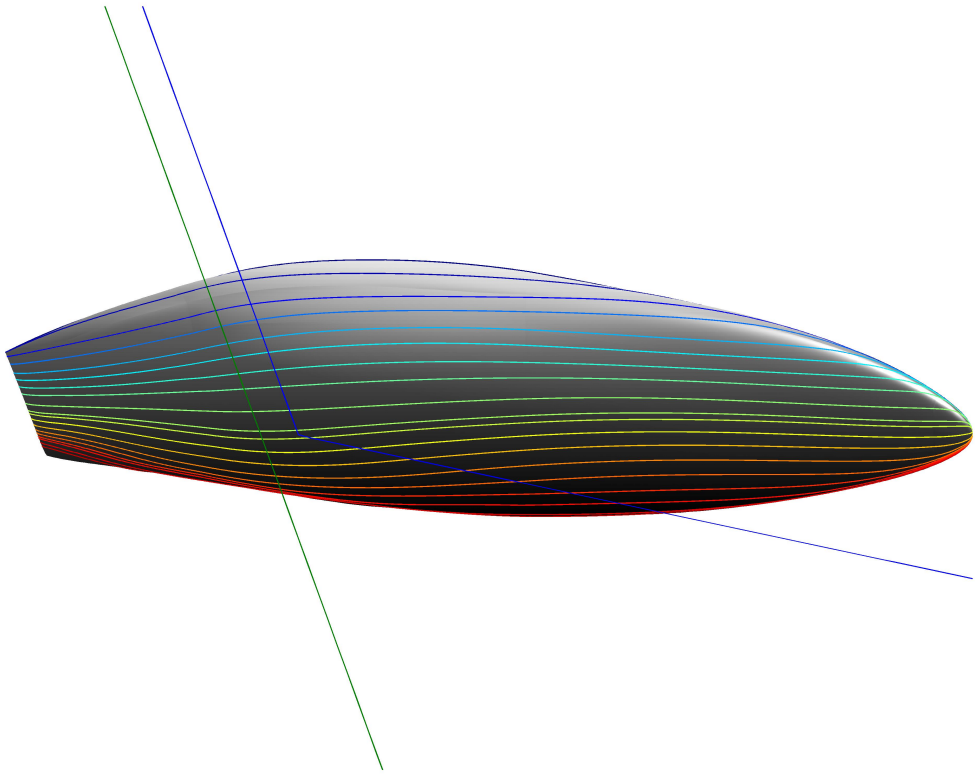

Figure 5.2: Surface streamlines across the final design point for *Eta*. The colours of the streamlines correspond to the colours in Figure 5.4. Note the lines indicating the desired transition point from a laminar to turbulent boundary layer and the desired point of the start of pressure recovery. For this flow solution, inviscid flow was assumed and $M_\infty = 0.1$.

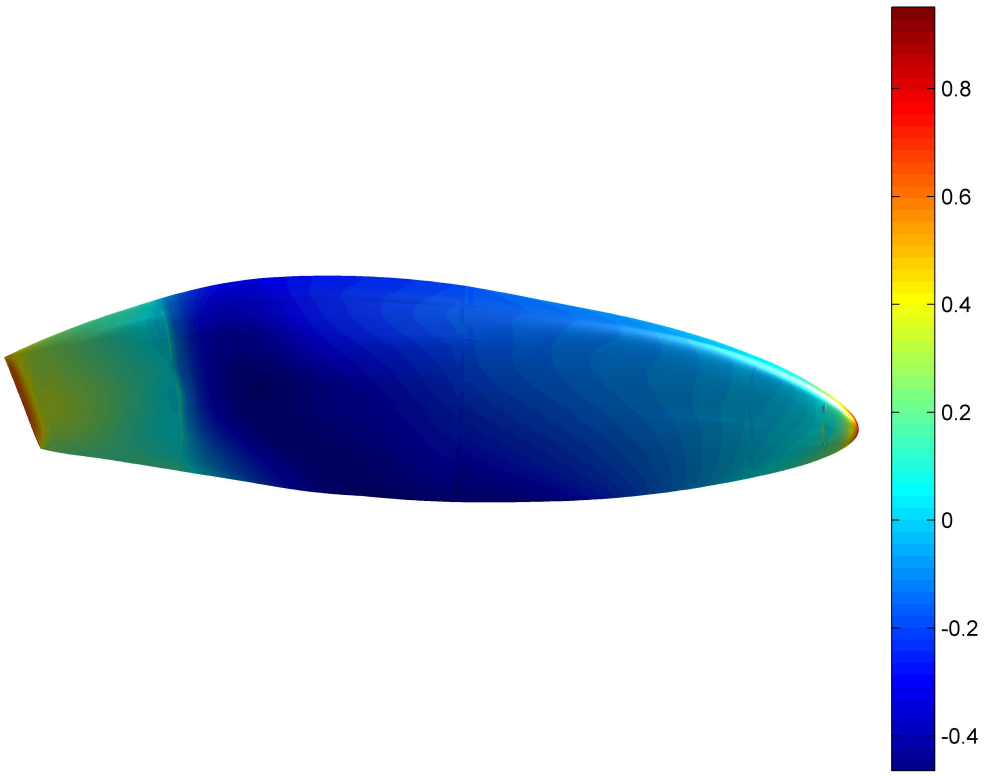

Figure 5.3: C_p distribution plotted on the surface of the final design point for *Eta*. For this flow solution, inviscid flow was assumed and $M_\infty = 0.1$.

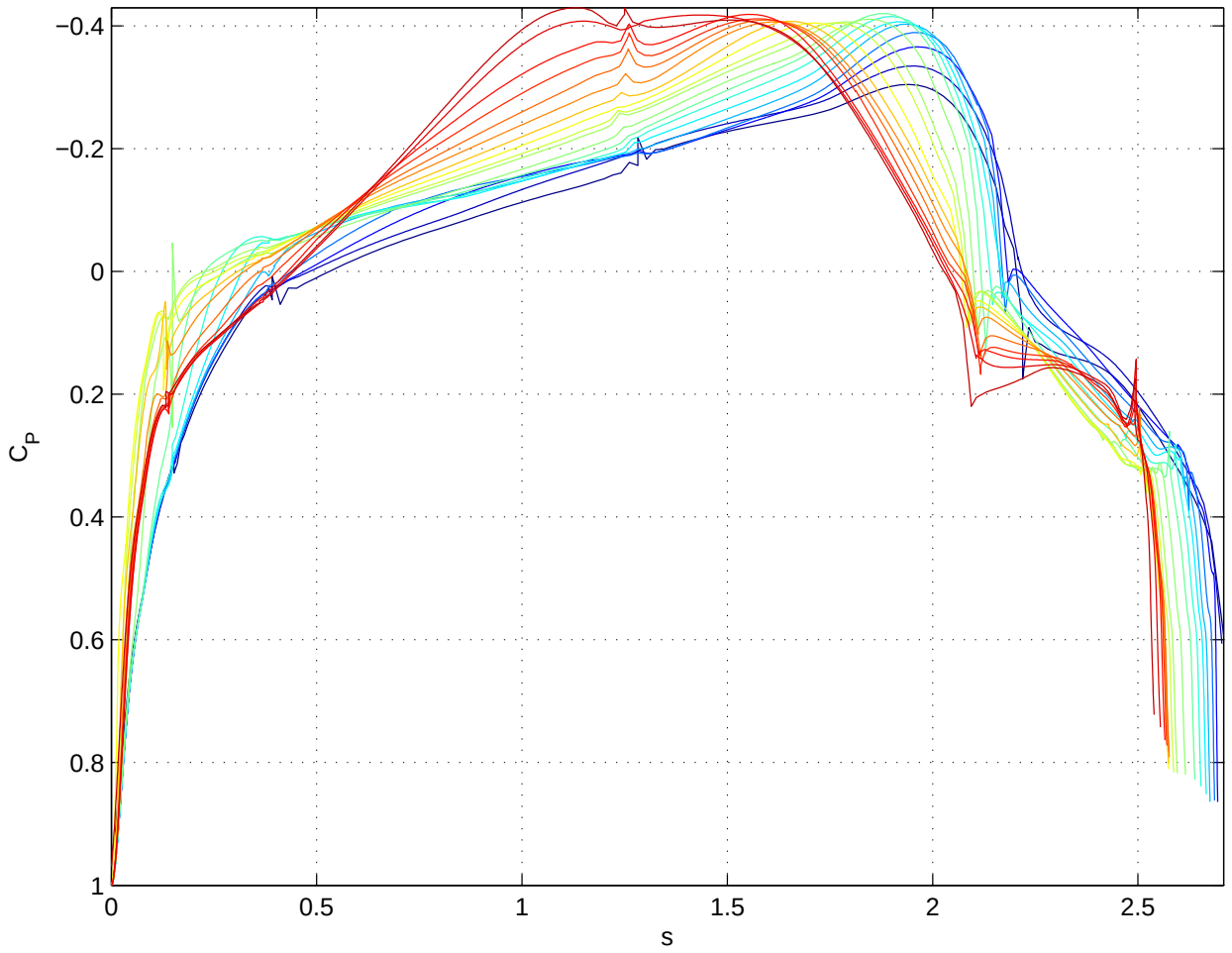

Figure 5.4: Pressure coefficient distribution, C_p verses streamline length, s across the aerodynamic surface of the final geometry. The streamline colours correspond to those shown in Figure 5.2. At the block interfaces, discontinuities can be seen in the flow solution. This is due to poor mesh refinement at the block interface however does not affect the quality of the global flow solution. ($M_\infty = 0.1$)

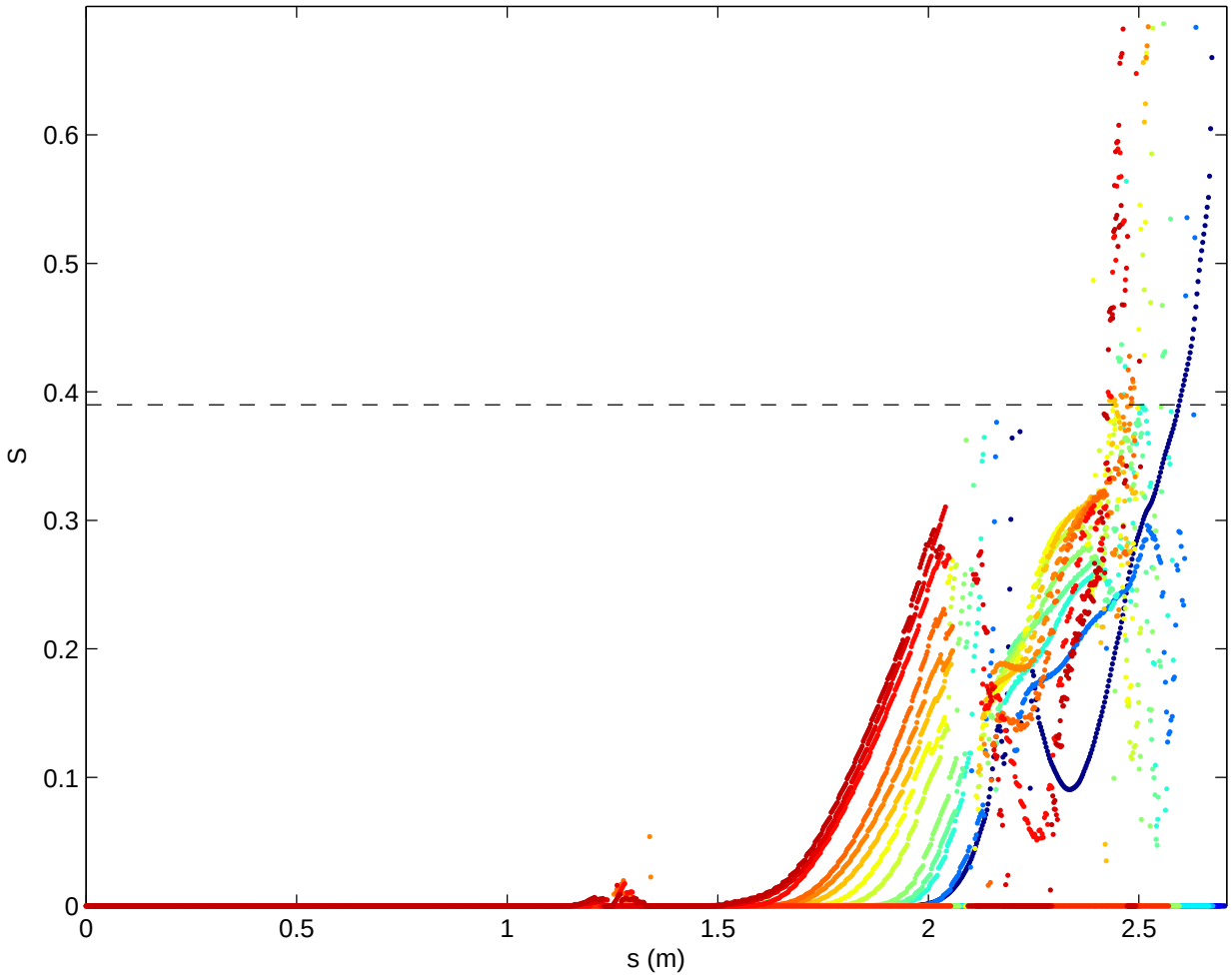

Figure 5.5: Stratford value, S verses streamline length, s across the aerodynamic surface of the final design point of *Eta*. For this analysis, $U_\infty = 50km/hr, \rho_\infty = 1.21kg/m^3$ and laminar flow is assumed until the transition line shown in Figure 5.2 or the point of $C_{p,min}$, whichever comes first. These conditions relate to the lowest Reynolds number deemed acceptable for flow separation on *Eta*. Note that the only region where the Stratford value exceeds 0.39 is near $s/\ell \approx 1$ where the analysis is not valid. Additionally, it may be noted that the discontinuities between block edges (as seen in Figure 5.4) have been removed for clarity as they are unphysical artifacts of the flow solution. These have been caused by poor mesh refinement at the block interface however they do not affect the quality of the global flow solution. For the flow solution, inviscid flow was assumed and $M_\infty = 0.1$.

5.2 Geometric Analysis

Figure 5.6 shows three-view drawings of the final geometry around the human model which serves as the internal geometric constraints for the design of *Eta*. The final shape of *Eta* satisfies all internal geometric constraints as was specified for the original geometry without modification.

It can be seen in Figure 5.6 that the rider's shoulders do protrude slightly from the sides of the vehicle however this is acceptable since the human model currently shows the nominal shoulder width of the University of Toronto's HPV Design Team's largest rider and the shoulders of this rider can be squeezed forward slightly to fit within the fairing. In fact, said rider fits within *Bluenose* which is $\sim 3.5cm$ narrower than the final design of *Eta* at the shoulders.

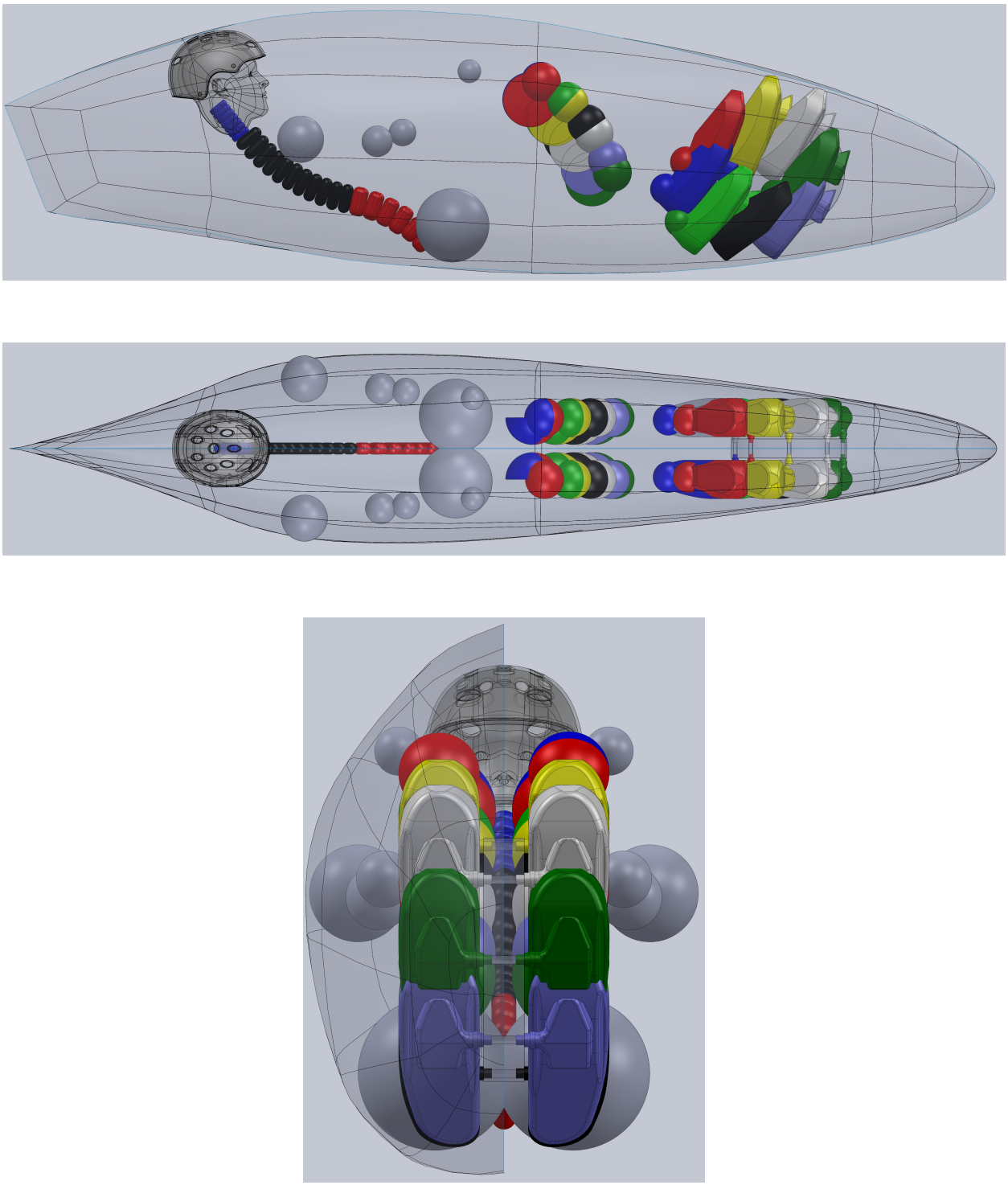

Figure 5.6: Three-view CAD drawings of the final geometry of *Eta* shown with a human model indicating the internal geometric constraints.

5.3 Drag Analysis

This section will discuss the aerodynamic drag analysis of an HPV to compare the design of *Eta* to that of *Bluenose*.

5.3.1 Analysis Method

To find the drag over an HPV, an empirical relation found in Hoerner for axisymmetric bodies extended for axisymmetric bodies with a flattened tail (as opposed to a conical tail) by Tamai will be used [11, 24]. Tamai's extension accounts for the reduction in boundary-layer pressure drag seen on a body with a flattened tail as opposed to one with a conical tail (assuming no separation) as well as a relation between the frontal area of a vehicle and the maximum diameter of an axisymmetric body with a flattened tail based upon empirical corrections from solar car data. The correlation presented in Tamai together with the induced drag on the vehicle can be seen below:

$$C_{d,wet} = C_{f,flat}\left(1 + 1.8\frac{(A_{front})^{0.75}}{L^{1.5}} + 0.39\frac{(A_{front})^{3}}{L^{6}}\right) + C_{d,i}\frac{A_{plan}}{A_{wet}} \tag{5.1}$$

where the induced drag coefficient, $C_{d,i}$, is output by *Jetstream* and $C_{f,flat}$ is the flat plate drag coefficient with the same transition point, x_t/L, as the actual vehicle.

The flat plate drag coefficient, $C_{f,flat}$, is found by applying the Blasius solution to the laminar region and using a momentum integral method together with empirically determined wall shear stress in the turbulent region, equating the boundary-layer thicknesses at the transition point as presented in Anderson [2].

5.3.2 Analysis Results

Results of the drag analysis on both *Bluenose* and *Eta* are shown in Table 5.1. The 21% reduction in drag coefficient is largely due to a larger extent of laminar flow for *Eta* over *Bluenose* and the overall 35% reduction in aerodynamic drag is additionally a product of the 18% reduction in wetted surface area of *Eta*. The $C_{d,i}$ term was negligible for both vehicles. C_dA is also plotted verses velocity for the two vehicles in Figure 5.7.

	Bluenose	*Eta*	
$C_{d,wet}$	0.0024	0.0019	**21%** drag coefficient reduction
A_{wet}	$4.26m^2$	$3.51m^2$	**18%** wetted area reduction
C_dA	$0.0104m^2$	$0.0068m^2$	**35% aerodynamic drag reduction**

Table 5.1: Drag comparison between *Bluenose* and *Eta* at $U_\infty = 100km/hr$ and $\rho = 1kg/m^3$.

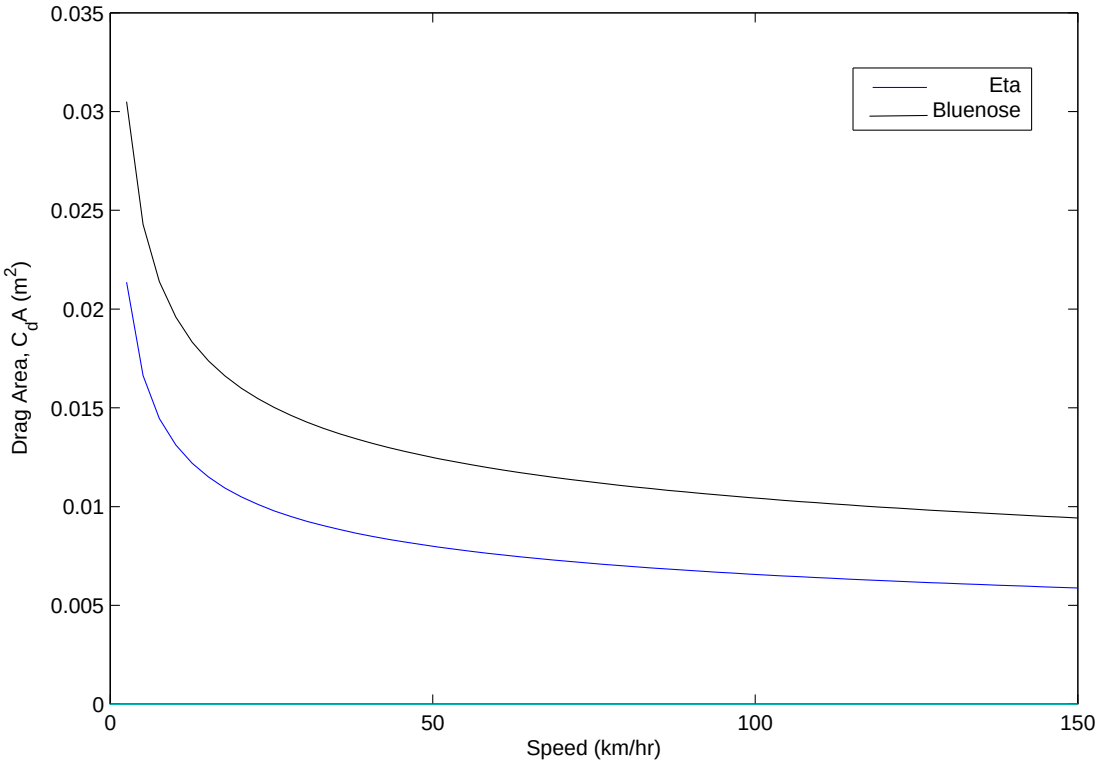

Figure 5.7: Comparison of Drag areas of *Bluenose* verses *Eta* over a range of U_∞ (assuming no boundary-layer separation). $\rho_\infty = 1kg/m^3$.

5.4 Performance Analysis

This section will analyze the performance of *Eta* in two competitions: the World Human-Power Speed Challenge where the vehicle speed is taken over $200m$ after an $8km$ flying start and a one-hour distance record attempt where the vehicle distance is measured from a standing start over one hour.

5.4.1 Analysis Method

In order to model the performance of *Eta* in the two competitions outlined above, the following will be taken into account in a numerical performance simulation:

Aerodynamic drag: the analysis used in §5.3 is used to model the drag over the body of *Eta*. Additionally, empirical corrections have be made for drag over wheel fairings, to account for ventilation and to account for surface cleanliness (door flanges, etc.).

Transmission efficiency: mechanical losses in transmission efficiency are estimated from [14].

Rolling resistance: rolling resistance data is estimated from [20] as well as from correlations found by the University of Toronto's HPV Design Team.

Inertial Effects: Vehicle/Rider mass and wheel rotational inertia are taken into account.

Competition Location: altitude density of race location as well as road slope (-0.8% grade at the World Human-Power Speed Challenge).

Rider Physiology: rider power output taken from power testing data of riders from the University of Toronto's HPV Design Team.

5.4.2 Analysis Results

Table 5.2 shows a summary of results from the competition performance simulation for both the World Human-Power Speed Challenge and a one-hour distance record attempt with *Eta*. It is evident that *Eta* promises substantial improvements over the current world record for both events. For the one-hour distance record attempt, a rider power output of $375W$ has been sustained whereas the power profile used for the World Human-Power Speed Challenge is shown in Figure 5.8.

World Human-Power Speed Challenge		**One-hour distance record attempt**	
(SR305, Battle Mountain, NV)		(Ford Michigan Proving Grounds, Romeo, MI)	
8km straight road		8km oval	
$\rho_\infty = 1kg/m^3$		$\rho_\infty = 1.13kg/m^3$	
Eta simulation:	**138.9km/hr**	*Eta* simulation:	**110km**
Existing Record:	133.78km/hr	Existing Record:	90.6km

Table 5.2: Summary of *Eta* performance simulation analysis for the World Human-Power Speed Challenge where the vehicles speed is taken over $200m$ after an $8km$ flying start and a one-hour distance record attempt where the vehicles distance is measured from a standing start over one hour.

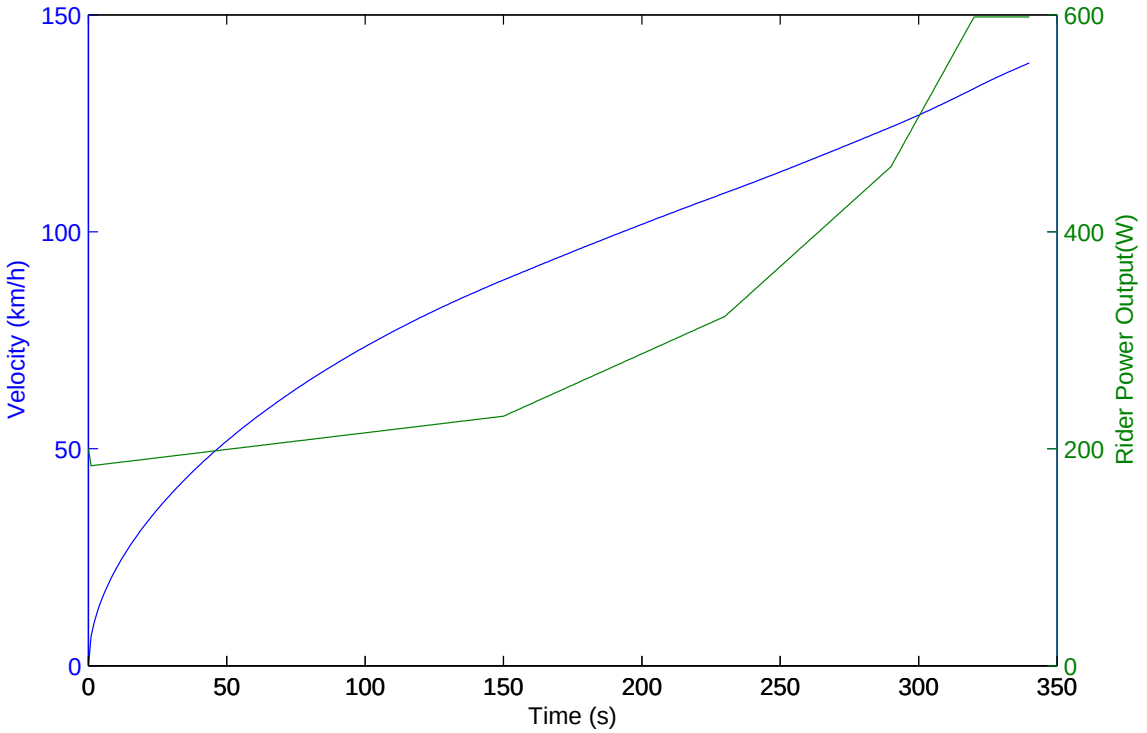

Figure 5.8: Rider power output and vehicle speed verses time for *Eta* at the World Human Power Speed Challenge.

Chapter 6

Conclusions and Future Work

The primary objective of this research is develop an improved design method for streamlined land vehicles and demonstrate its effectiveness on the design of a new human-powered vehicle. This chapter will concisely present the findings of this research as well as possible future extensions of this design method from the groundwork laid in this report.

6.1 Concluding Remarks

To reiterate the proposed inverse aerodynamic design method presented in this report, (described in more detail in §4.1) the design process can be outlined as follows:

1. Determine geometric constraints of all internal objects which must be placed within the vehicle with CAD software.
2. Determine a preliminary aerodynamic shape around the body using CAD software.
3. Solve the Euler equations around the preliminary vehicle shape in *Jetstream*.
4. Analyze the pressure distribution over the body along surface streamlines.
5. Determine the desired pressure distribution which satisfies the amount of laminar flow required but is similar to the pressure distributions at the previous design point. Output this target pressure distribution for the inverse optimization case.
6. Run the inverse optimization case in *Jetstream* until satisfactory convergence.
7. Return to step 4. Iterate if necessary until the current design point is satisfactory, meeting all constraints and aerodynamic goals.

This method has been used to design *Eta* whose progress was outlined in detail throughout §4. §5 then continues to critique the final design and compare its drag to the reference design, *Bluenose*, then continues to estimate the competition performance of the fully constructed vehicle.

The design of *Eta* has shown to be have a substantial reduction in both user interface time as well as design lead time compared to the design of *Bluenose*. While the aerodynamic design of *Bluenose* took $\sim$ 2 months and about 35 design iterations, (a design iteration being a loop of the scheme described in §2.2) the design of *Eta* took effectively 2 days of setup (the majority involved with finding the original design point and meshing the computational domain) together with $\sim$ 20 hours of runtime for the optimization process on 32 processors. This substantial reduction in the design time can not only help to compress a project schedule but also makes the design method conducive to rapid design sweeps. Even with this substantial reduction in the design timeline, a superior human-powered vehicle has been designed with a 35% reduction in aerodynamic drag over *Bluenose*.

Eta will be constructed over the summer of 2014 by the University of Toronto's HPV Design Team together with AeroVelo and will be tested in the same competition scenarios presented in §5.4 where *Eta* has shown promise in breaking both the IHPVA world cycling speed record and one-hour distance record by a large margin. The on-road performance of the constructed vehicle will be the ultimate test of its design methodology.

6.2 Future Work

This section will describe some potential extensions of the design method researched in this report. They would likely be greatly beneficial from a design and research perspective however it was not possible to explore them within the timeline of the project.

6.2.1 Derivation of Actual from Effective Body

Since the Euler equations are being solved for the design method proposed, viscous effects are not considered in the flow solution however the thickness of the boundary layer does change the "effective" shape of the body.

To give an idea of the shape change at the Reynolds numbers most streamlined vehicles operate at, the boundary-layer displacement thickness, δ^*, can be approximated by the flat plate model presented by Anderson [2]. For the size and operating conditions of an HPV, $\delta^* \approx 1.5$ cm and for a solar car, $\delta^* \approx 2.4$ cm at the trailing edge. While this is not a substantial shape change it could certainly be accounted for to achieve a more accurate final

shape.

This could be accounted for by assuming the shape of the aerodynamic surface defined by the mesh in the flow is the "effective" shape of the vehicle and the goal is to back out the "actual" shape to ensure it satisfies the geometric constraints of the vehicle's internals. This can be done by calculating δ^* along the streamlines and interpolating δ^* across the rest of the surface at which point the actual body shape can be determined by offsetting the mesh surface by δ^* inwards in the surface normal direction. δ^* can be calculated by one of two ways, the second being the most accurate:

1. δ^* can be found along streamlines by ignoring the pressure gradient and approximating its thickness to that of a flat plate with a partly turbulent, partly laminar boundary layer through relations presented by Anderson [2].

2. δ^* can be calculated by solving the boundary-layer equations [2], given the pressure distribution along the streamlines. This could be conducted through XFOIL [5].

6.2.2 Design for Appendages

Appendages which could be present on a streamlined land vehicle include wheel fairings, vertical stability surfaces, sailing surfaces or a bubble canopy. These appendages will have some effect on the performance of the HPV and will affect the pressure distribution of the body, especially near the appendage attachment point. Due to the complex nature of the flow around appendages, it is unlikely that a pressure profile parameterization scheme used for the rest of the body could be utilized for streamlines around the appendages. Instead a more modular solution would likely need to be applied. Such a method could include allowing the user to modify the pressure profile around the appendage in a more hands-on approach by playing with control points of B-spline curves. The rest of the process described in §4 will largely remain the same except the streamlines around appendages would be treated differently.

For the design of the HPV being conducted in this research project, the appendages will be omitted for simplicity. This will likely not affect the pressure distribution on the body greatly since the wheel fairings which will be employed on the final vehicle will be very narrow. Still, it would be preferable to design with the fairings in mind.

6.2.3 Implementation of Additional Geometric Constraints

An additional constraint which would be practical for the shape optimization (in addition to the C^1 edge constraint discussed in §4.4.6) would be to constrain the surface to be normal to

the symmetry plane where it intersects it. While there is functionality for this constraint implemented in *Jetstream*, it was not successful utilized for the design of *Eta*. Additionally, C^2 edge constraints would be ideal for the final surface of a streamlined land vehicle since curvature continuity is important for NLF however this has yet to be successfully integrated into *Jetstream*.

References

[1] I. H. Abbot and A. E. Von Doenhoff, *Theory of Wing Sections Including a Summary of Airfoil Data*, General Publishing Company, Toronto, 1959.

[2] J. D. Anderson, *Fundamentals of Aerodynamics*, McGraw-Hill, 1991.

[3] M. Drela, *Mark Drela's quoted rules of thumb.* `www.recumbents.com/WISIL/barracuda/barracudafairingdesign.htm`.

[4] M. Drela, *All-sealed fairings: Ventilation gives very low drag*, Technical Journal of the IHPVA, 11 No. 3 (1994), p. 23.

[5] M. Drela and H. Youngren, *XFOIL 6.9 user primer.* `http://web.mit.edu/drela/Public/web/xfoil/xfoil_doc.txt`, Nov, 2001.

[6] D. Fudge, D. W. Zingg, and R. Haimes, *A CAD-free and a CAD-based geometry control system for aerodynamic shape optimization.*, AIAA Paper 2005-0451, (January 2005).

[7] P. Garrison and D. F. Pinella, *Cmarc.* AeroLogic. `http://www.aerologic.com/cmarc.html`.

[8] P. E. Gill, W. Murray, and M. A. Saunders, *SNOPT: An SQP algorithm for large-scale constrained optimization*, SIAM Review, 47 (2005), pp. 99–131.

[9] J. E. Hicken, *Efficient Algorithms for Future Aircraft Design: Contributions to Aerodynamic Shape Optimization*, PhD thesis, Graduate Department of Aerospace Science and Engineering, University of Toronto, 2009.

[10] J. E. Hicken and D. W. Zingg, *Parallel Newton-Krylov solver for the Euler equations discretized using simultaneous-approximation terms.*, AIAA Journal, 46 (2008), pp. 2773–2786.

[11] S. F. Hoerner, *Fluid-Dynamic Drag*, Published by author, Hoerner Fluid Dynamics, Brick Town, N. J., USA, 1965.

[12] International Human-Powered Vehicle Association, *IHPVA Official Speed Records: Land.* `http://www.ihpva.org/hpvarec3.htm#nom27`.

[13] J. Katz and A. Plotkin, *Low-Speed Aerodynamics*, Cambridge University Press, 2001. Second Edition.

[14] M. D. Kidd, *Bicycle Chain Efficiency*, PhD thesis, Heriot-Watt University Edinburgh, 2000.

[15] C. R. Kyle and M. D. Weaver, *Aerodynamics of human-powered vehicles*, Proceedings of the Institution of Mechanical Engineers, Part A: Journal of Power and Energy., (2004).

[16] M. Mowett, *Fastest human list records.* `http://www.wisil.recumbents.com/wisil/fastest_list.asp`.

[17] M. Nemec, *Optimal Shape Design of Aerodynamic Configurations: A Newton-Krylov Approach*, PhD thesis, Graduate Department of Aerospace Science and Engineering, University of Toronto, 2003.

[18] M. Nemec and D. W. Zingg, *A Newton-Krylov Algorithm for Aerodynamic Design using the Navier-Stokes Equations.*, AIAA Journal, 40 (2002), pp. 1146–1154.

[19] T. Reichert, *Aerodynamic design of the vortex human-powered land-speed vehicle.* 2011.

[20] W. Schermer, *Tire rolling resistance pendulum tests.* 2012.

[21] H. Schlichting, *Boundary-Layer Theory*, McGraw-Hill, 1979.

[22] A. M. O. Smith, *Stratford's turbulent separation criteria for axially symmetric flows*, Journal of Applied Mathematics and Physics, 28 (1977).

[23] B. S. Stratford, *The prediction of the turbulent boundary layer*, National Gas Turbine Establishment, (July 17, 1958).

[24] G. Tamai, *The Leading Edge: Aerodynamic Design of Ultra-Streamlined Land Vehicles*, Bentley Publishers, Cambridge, MA, USA, 1999.

[25] Unknown, *VSAERO.* Analytical Methods. `http://www.am-inc.com/VSAERO.shtml`.

[26] C. P. Van Dam and P. M. H. W. Vijgen, *Design of fuselage shapes for natural laminar flow*, Nasa Contractor Report 3970, (1986).

[27] M. Weaver, *Speed 101.* `www.speed101.com`, 2003.

Appendices

Appendix A

Update: Parameterization Revision

This update was conducted May 29, 2014.

Before the construction of *Eta*, a second design iteration had been made. This was largely due to a design change of the vehicle wheel size and rider ergonomics which changed the internal rider constraints (the new internal constraints can be seen in figure A.3). Details into the geometry change and optimization setup will not be made here as it is not relevant to the design process outlined in this research project however there was a slight change which was made to the parameterizations of the streamlines which will be noted.

As seen in figure A.1, an additional parameter had been added to the streamline pressure profile parameterization and optimization scheme described in §4.3.3. This additional parameter has allowed the streamlines on the bottom of the vehicle (which transition early) to begin a gentle pressure recovery before the specified recovery region. This difference can be seen by comparing figure A.1 to figure 4.10 where the pressure coefficient on the bottom streamlines remain constant before the pressure recovery region. This modification was advantageous for several reasons:

1. The previous parameterization scheme often required unnecessary flow overspeeds on the bottom of the vehicle to match the pressure distribution over the previous geometry in a least squares sense. This required a more aggressive pressure recovery and higher viscous drag over the overspeeded region.

2. The early recovery allows pressure relief earlier then the previous parameterization allowed. This reduced the overspeeded flow seen in this region and thus reduced the viscous drag.

3. The gentle early pressure recovery can reduce how aggressive the final pressure recovery is because the C_P will be higher at that point.

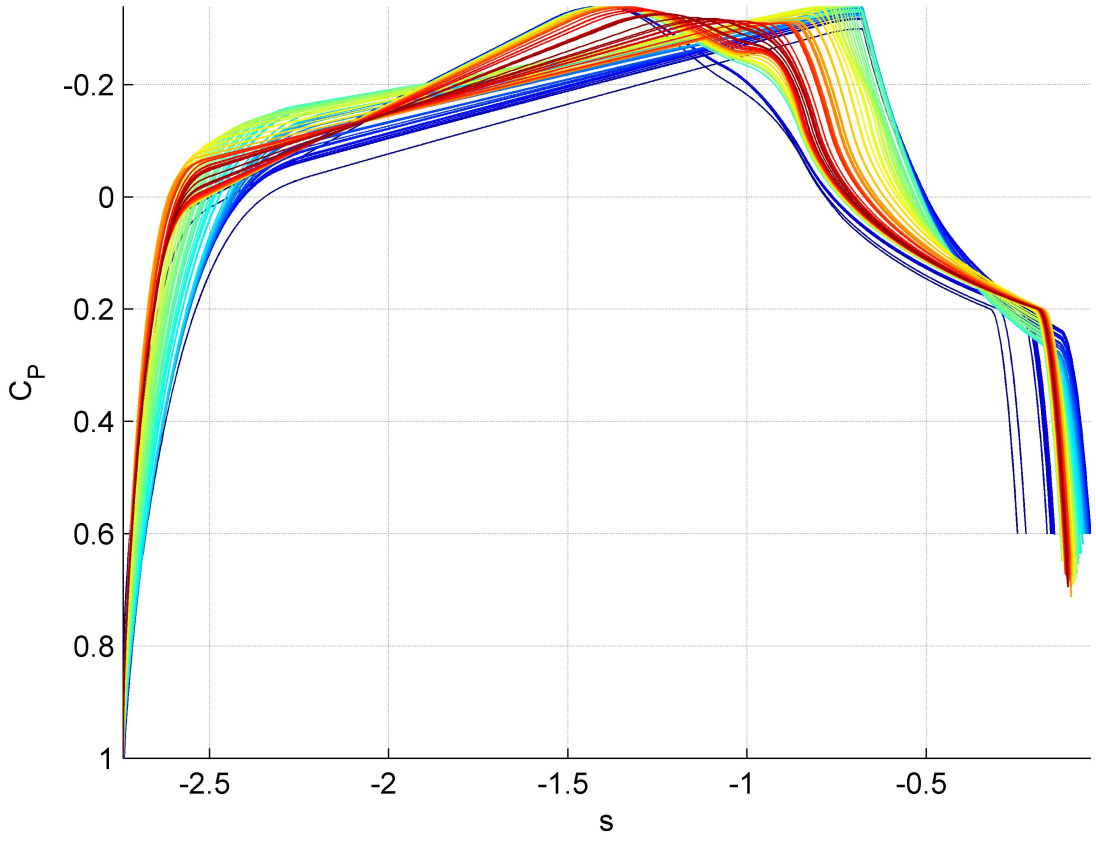

Figure A.1: Ideal pressure coefficient distribution, $C_{p,ideal}$, verses streamline length, s found for the original design point of *Eta* for the second iteration.

As a result of this new parameterization, the ideal pressure coefficient surface distribution for the second *Eta* iteration can be seen in figure A.2. After optimizations the final vehicle shape can be seen in figure A.3 and the final surface streamline pressure coefficient distribution can be seen in figure A.4 after the wheel well appendages had been added.

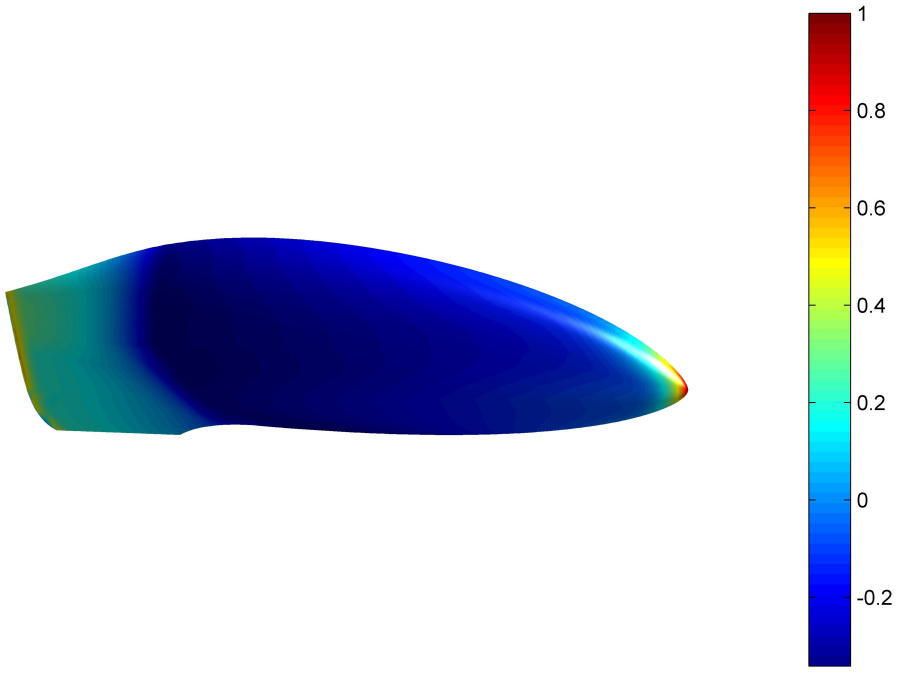

Figure A.2: Ideal pressure coefficient distribution, $C_{p,ideal}$, found for the original design point of the second iteration of *Eta* projected on the original design point geometry.

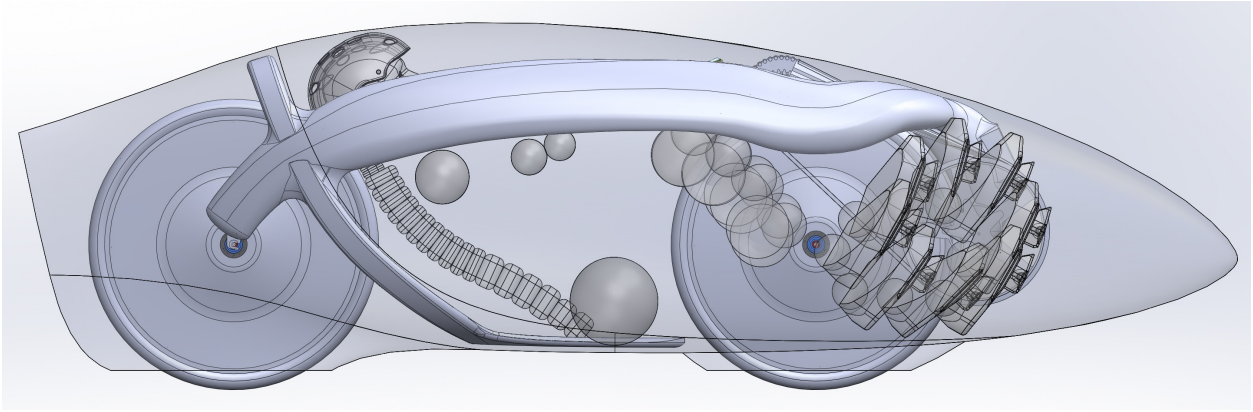

Figure A.3: The new rider configuration of *Eta* for the final design iteration.

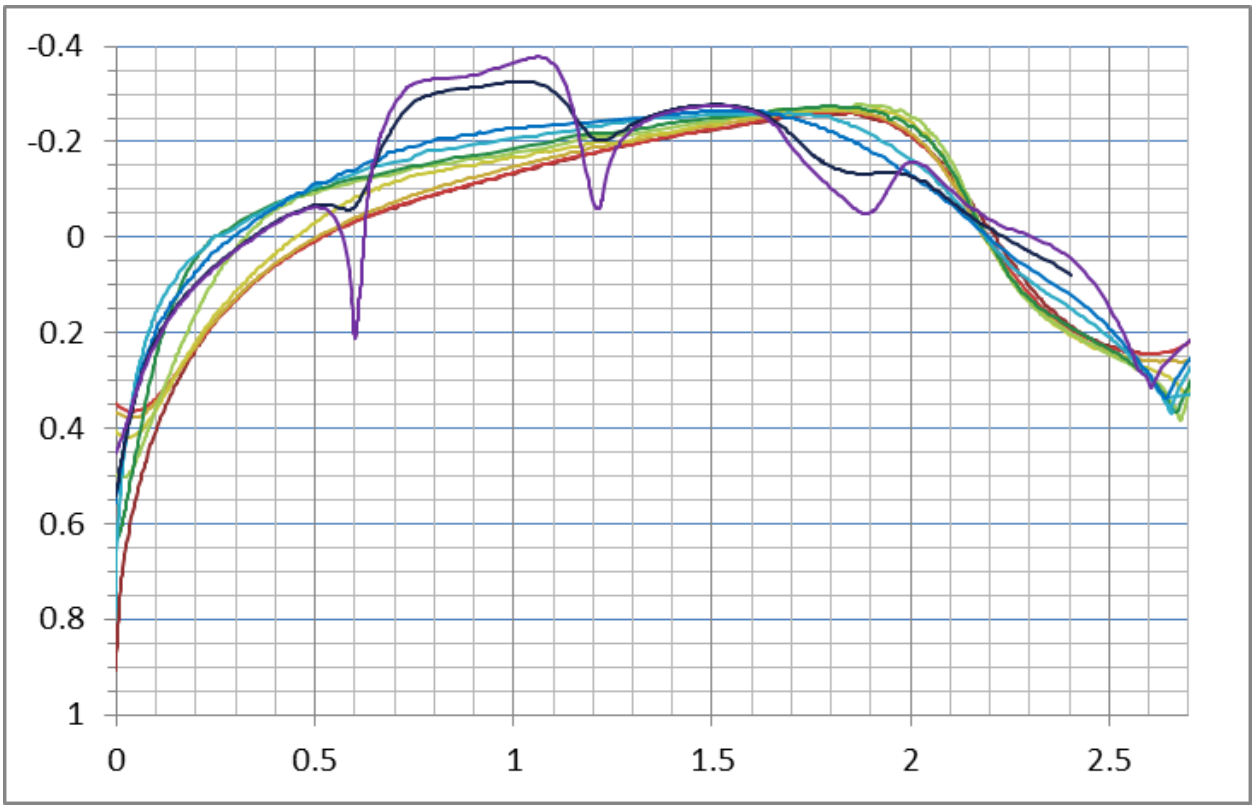

Figure A.4: Pressure coefficient distribution over the surface streamlines of *Eta* after the final design iteration. This simulation had been conducted after the appendages were added to the model. ($M_\infty = 0.1$)

Appendix B

Update: *Eta* Completion

This update was conducted September 20, 2014.

Over the summer of 2014, AeroVelo constructed *Eta* in an attempt to break the International Human-Powered Vehicle Association's world land-speed record at the World Human-Powered Speed Challenge in Battle Mountain, Nevada. Based upon available rider power and on-road power data, *Eta* appears to be capable of speeds over 140 km/hr at the the World Human-Powered Speed Challenge however *Eta* did not yet reach its full speed potential due to numerous mechanical issues. AeroVelo will be returning to the competition in September, 2015 with these issues sorted. Despite these issues, *Eta* still reached a top speed of 127 km/hr. Images of the completed vehicle can be seen in figures B.1, B.2 and B.3.

Figure B.1: The final, constructed *Eta* running at the World Human-Powered Speed Challenge in Battle Mountain, Nevada in September, 2014. *Eta* reached a speed of 127km/hr however did not yet reach its full speed potential to numerous mechanical issues.

Figure B.2: The final, constructed *Eta* being launched at the World Human-Powered Speed Challenge in Battle Mountain, Nevada in September, 2014. *Eta* reached a speed of 127km/hr however did not yet reach its full speed potential to numerous mechanical issues.

Figure B.3: The final, constructed *Eta* with the AeroVelo team at the World Human-Powered Speed Challenge in Battle Mountain, Nevada in September, 2014. *Eta* reached a speed of 127km/hr however did not yet reach its full speed potential to numerous mechanical issues.